Monthly Notices
of the
ROYAL ASTRONOMICAL SOCIETY
MNRAS **441,** 2891–2922 (2014) doi:10.1093/mnras/stu387

The ALHAMBRA Survey: Bayesian photometric redshifts with 23 bands for 3 deg^2

A. Molino,[1⋆] N. Benítez,[1] M. Moles,[2] A. Fernández-Soto,[3,4] D. Cristóbal-Hornillos,[2] B. Ascaso,[1] Y. Jiménez-Teja,[1] W. Schoenell,[1] P. Arnalte-Mur,[5] M. Pović,[1] D. Coe,[6] C. López-Sanjuan,[2] L. A. Díaz-García,[2] J. Varela,[2] M. Stefanon,[7] J. Cenarro,[2] I. Matute,[1] J. Masegosa,[1] I. Márquez,[1] J. Perea,[1] A. Del Olmo,[1] C. Husillos,[1] E. Alfaro,[1] T. Aparicio-Villegas,[1,8] M. Cerviño,[1,9] M. Huertas-Company,[10,11] J. A. L. Aguerri,[9] T. Broadhurst,[12] J. Cabrera-Caño,[13] J. Cepa,[9,14] R. M. González,[1] L. Infante,[15] V. J. Martínez,[4,16,17] F. Prada[1] and J. M. Quintana[1]

Affiliations are listed at the end of the paper

Accepted 2014 February 25. Received 2014 February 25; in original form 2013 June 24

ABSTRACT

The Advance Large Homogeneous Area Medium-Band Redshift Astronomical (ALHAMBRA) survey has observed eight different regions of the sky, including sections of the Cosmic Evolution Survey (COSMOS), DEEP2, European Large-Area Infrared Space Observatory Survey (ELAIS), Great Observatories Origins Deep Survey North (GOODS-N), Sloan Digital Sky Survey (SDSS) and Groth fields using a new photometric system with 20 optical, contiguous ∼300-Å filters plus the *JHKs* bands. The filter system is designed to optimize the effective photometric redshift depth of the survey, while having enough wavelength resolution for the identification of faint emission lines. The observations, carried out with the Calar Alto 3.5-m telescope using the wide-field optical camera Large Area Imager for Calar Alto (LAICA) and the near-infrared (NIR) instrument Omega-2000, represent a total of ∼700 h of on-target science images. Here we present multicolour point-spread function (PSF) corrected photometry and photometric redshifts for ∼438 000 galaxies, detected in synthetic $F814W$ images. The catalogues are complete down to a magnitude $I \sim 24.5$ AB and cover an effective area of 2.79 deg^2. Photometric zero-points were calibrated using stellar transformation equations and refined internally, using a new technique based on the highly robust photometric redshifts measured for emission-line galaxies. We calculate Bayesian photometric redshifts with the Bayesian Photometric Redshift (BPZ)2.0 code, obtaining a precision of $\delta_z/(1+z_s) = 1$ per cent for $I < 22.5$ and $\delta_z/(1+z_s) = 1.4$ per cent for $22.5 < I < 24.5$. The global $n(z)$ distribution shows a mean redshift $\langle z \rangle = 0.56$ for $I < 22.5$ AB and $\langle z \rangle = 0.86$ for $I < 24.5$ AB. Given its depth and small cosmic variance, ALHAMBRA is a unique data set for galaxy evolution studies.

Key words: methods: data analysis – techniques: photometric – catalogues – surveys – galaxies: distances and redshifts – galaxies: evolution – galaxies: photometry.

1 INTRODUCTION

Photometric redshifts (Baum 1962; Lanzetta, Fernández-Soto & Yahil 1996; Benítez 2000) have become a powerful tool for cosmology and galaxy evolution studies. Several medium-band photometric surveys have been carried out in the last years: the University of British Columbia–National Aeronautics and Space Administration (UBC–NASA) survey (Hickson & Mulrooney 1998), Calar Alto Deep Imaging Survey (CADIS: Wolf, Meisenheimer & Roser 2001b), Classifying Object by Medium-Band Observatins in 17 Filters (COMBO-17: Wolf et al. 2001a) and most recently, the Cosmic Evolution Survey (COSMOS-21: Taniguchi et al. 2005; Ilbert et al. 2009), National Optical Astronomy Observatory Extremely Wide-Field Infrared Imager (NEWFIRM: van Dokkum et al. 2009) and Survey for High-z Absorption Red and Dead Sources (SHARDS:

⋆ E-mail: amb@iaa.es

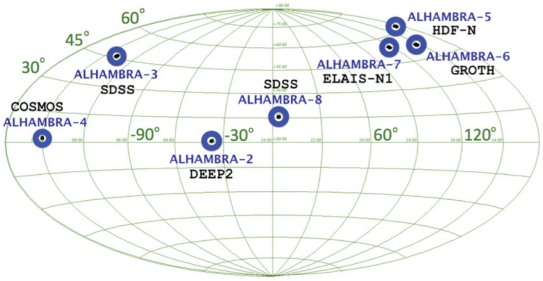

Figure 1. The figure shows the different fields observed by the ALHAMBRA survey, along with their correspondence with other existing surveys. The mean Galactic coordinates are specified in Table 1.

Pérez-González et al. 2013). The Advance Large Homogeneous Area Medium-Band Redshift Astronomical (ALHAMBRA) survey (Moles et al. 2008) has been optimized to detect and measure precise and reliable photometric redshifts for a large population of galaxies over eight different fields. Broad-band photometric surveys can be significantly shallower, in terms of photometric redshift depth, than well-designed, medium-band imaging (see Wolf et al. 2001a; Benítez et al. 2009b, for a systematic study). ALHAMBRA uses a specially designed filter system (see also Aparicio-Villegas et al. 2010) that covers the whole optical range (3500–9700 Å) with 20 contiguous, equal-width, non-overlapping, medium-band filters along with the standard *JHKs* near-infrared bands. The initial goal of the project was to cover a total area of 4 deg^2 on the sky divided into eight non-contiguous regions (Fig. 1).

The photometric system has been specifically designed to optimize photometric redshift depth and accuracy (Benítez et al. 2009b), while having enough sensitivity for the detection and identification of faint emission lines (Bongiovanni et al. 2010; Matute et al. 2012; Matute et al. 2013). The observations presented here were carried out with the Calar Alto 3.5-m telescope using both the wide-field Large Area Imager for Calar Alto (LAICA) camera in the optical range and the Omega-2000 camera in the near-infrared (NIR) from 2005–2012. In order to define a constant and homogeneous window for all ALHAMBRA fields, we generated synthetic *F*814*W* detection images (corresponding to *Hubble Space Telescope* (*HST*)/Advanced Camera for Surveys (ACS) *F*814*W*). These images are photometrically complete down to a magnitude $m_{F814W} \leq 24.5$, have a much better signal-to-noise ratio (S/N) than individual filters and allow direct comparisons with other space-based surveys such as COSMOS. Hereafter, m_{F814W} magnitudes correspond to the magnitudes derived for the synthetic *F*814*W* images.

In this article, we summarize the ALHAMBRA survey observations and data reduction in Section 2. In Section 3, we describe in detail the photometric catalogues used to derive photometric redshifts. This includes aperture-matched point-spread function (PSF) corrected photometry, the generation of synthetic *F*814*W* detection images and their corresponding star masking treatment, a statistical star/galaxy classification and an empirical estimation of the photometric uncertainties. We discuss several photometric checks in Section 3.8. In Section 4 we analyse the methodology used to derive the photometric redshifts, the different methods used to compute photometric zero-point calibrations and the photometric redshift accuracy quantification as a function of *F*814*W* magnitude, redshift and *Odds*. Finally, we present a description of the ALHAMBRA photometric redshift catalogues in Section 5.

All optical and NIR magnitudes in this article are in the AB system. Cosmological parameters of $H_0 = 70\,\mathrm{km\,s^{-1}\,Mpc^{-1}}$, $\Omega_\mathrm{M} = 0.3$ and $\Omega_\Lambda = 0.7$ are assumed throughout.

2 OBSERVATIONS AND DATA REDUCTION

2.1 Observations

The ALHAMBRA survey has imaged a total area of 4.0 deg^2 in eight separated regions of the sky during a seven-year period (2005–2012). Observations were carried out with the 3.5-m telescope at the Calar Alto Observatory (CAHA, Spain), making use of the two wide-field imagers in the optical (LAICA) and NIR (Omega-2000). The ALHAMBRA fields have been observed whenever the conditions were good (seeing <1.6 arcsec, airmass <1.8), for a total on-target exposure time of ∼700 h for the whole survey, corresponding to ∼32 h for each field. The integration time was split into ∼27.8 h for medium-band filters and ∼4.2 h for broad-band NIR filters, as explained in Cristobal-Hornillos et al. (in preparation).

Although ALHAMBRA-01 has already been observed, its analysis has not been included in this article owing to issues with its primary photometric calibration at the time. For a detailed description of the NIR observations, we refer the reader to Cristóbal-Hornillos et al. (2009). The description of the optical observations will be available in Cristobal-Hornillos et al. (in preparation).

2.2 Data reduction

In order to homogenize the data sets from both imagers, NIR images from the OMEGA-2000 detector were converted from their original pixel size, 0.45 arcsec pixel^{-1}, to 0.221 arcsec pixel^{-1} to match the pixel size of the LAICA images. As explained in Cristóbal-Hornillos et al. (2009), individual images from each run have been dark-current-corrected, flat-fielded and sky-subtracted. Bad pixels, cosmic rays, linear patterns and ghost images have also been masked out. Processed images have been finally combined using the SWARP (Bertin et al. 2002) software and the applied geometrical transformations have been incorporated in World Coordinate System (WCS) headers.

The total 2.8 deg^2 considered in this work is divided into seven non-contiguous regions of the sky (as summarized in Table 1), each of which is split into two non-overlapping strips composed of four individual CCDs, as schematically illustrated in Appendix A. Each one of the 48 CCDs represents the minimum area (15.5 × 15.5 arcmin^2) covered by all 23 individual filters. To quantify the survey effective area (Section 3.5.3), FLAG images have been created where pixels not satisfying established photometry quality criteria have been flagged. Meanwhile, both RMS-map and WEIGHT-maps have been generated, accounting for the level of photometric uncertainties present across individual images.

2.3 Filter set

Once the instrumental set-up and exposure time are fixed, the filter set has a powerful effect on the photometric redshift (photo-z) performance (see Wolf et al. 2001a; Benítez et al. 2009b). Table 2 summarizes a small list of different photometric filter systems and their photometric redshift accuracy. The ALHAMBRA survey designed its own photometric system (Benítez et al. 2009b) optimizing both photometric depth and accuracy. As seen in Fig. 2, the system covers the 3500–9700 Å optical window with 20 constant-width (∼300 Å), non-overlapping filters. We also use the *J*, *H* and *Ks* NIR bands. Including both optical and NIR observations helps to break colour–redshift degeneracies, reducing the fraction of catastrophic outliers and increasing the ALHAMBRA photometric redshift depth. In Fig. 3, we show a galaxy observed through the whole

Table 1. The ALHAMBRA survey selected fields.

Field name	Overlapping survey	RA (J2000)	Dec. (J2000)	Area/Effective [deg^2]	Number of catalogues	Science images	Detected [a] sources	Density [a,b] [#/deg^2]
ALHAMBRA-1	–	00 29 46.0	+05 25 30	0.50/–	–	192	–	–
ALHAMBRA-2	DEEP2	01 30 16.0	+04 15 40	0.50 / 0.45	8	192	67.791	77.144
ALHAMBRA-3	SDSS	09 16 20.0	+46 02 20	0.50 / 0.47	8	192	68.015	75.000
ALHAMBRA-4	COSMOS	10 00 00.0	+02 05 11	0.25 / 0.23	4	96	38.464	93.261
ALHAMBRA-5	HDF-N	12 35 00.0	+61 57 00	0.25 / 0.24	4	96	42.618	82.300
ALHAMBRA-6	GROTH	14 16 38.0	+52 24 50	0.50 / 0.47	8	192	66.906	77.740
ALHAMBRA-7	ELAIS-N1	16 12 10.0	+54 30 15	0.50 / 0.47	8	192	79.453	82.185
ALHAMBRA-8	SDSS	23 45 50.0	+15 35 05	0.50 / 0.46	8	192	75.109	82.452
				3.00 / 2.79	48	1344	438.356	⟨81.440⟩

[a]Without duplications.
[b]$m_{F814W} < 24$.

Table 2. Photometric redshift surveys. Since, for narrow/medium-band photometric surveys (*), the photometric redshift accuracy is strongly dependent on the S/N, we compared the performance from both surveys applying a similar cut in magnitude ($R < 23$ AB for COMBO-17 and $I < 23$ AB for ALHAMBRA). For the brightest sources, both surveys reach a performance similar to that of COSMOS or the Multiscale Systems Center (MUSYC) $\delta_z/(1+z) < 0.01$.

Survey	Reference	Bands	$\delta_z/(1+z)$
HDF	Sawicki, Lin & Yee (1997)	4	0.080
SDSS/DR6	Csabai et al. (2003)	5	0.035
SWIRE	Rowan-Robinson et al. (2008)	5	0.035
HUDF	Coe et al. (2006)	6	0.040
HDF	Fernández-Soto, Lanzetta & Yahil (1999)	7	0.060
CFHTLS	Ilbert et al. (2006)	9	0.030
GOODS	Dahlen et al. (2010)	12	0.040
CLASH	Molino (in prep.)	16	0.025
COMBO-17*	Wolf et al. (2008)	17	0.020
ALHAMBRA*	Molino (this work)	23	0.010
COSMOS	Ilbert et al. (2009)	30	0.007
MUSYC	Cardamone et al. (2010)	32	0.007
JPAS	Benítez et al. (2009a, 2014, in prep.)	59	0.003

ALHAMBRA filter system. The main properties of each individual filter are summarized in Table 3.

2.4 Primary photometric zero-point calibration

A set of transformation equations between the ALHAMBRA and the SDSS (York et al. 2000) was derived based on a collection of primary standard stars from the *HST*/Space Telescope Imaging Spectrograph (STIS) Next Generation Spectral Library (NGSL: Gregg et al. 2004), as explained in Aparicio-Villegas et al. (2010).

We applied these equations to all stars with good photometry in both ALHAMBRA and the SDSS/DR7 data and derived photometric zero-points from the mean differences between instrumental and synthetic magnitudes, yielding an internal error no larger than a few hundredths of a magnitude for stars in each CCD and filter combination. For an in-depth discussion of the calibration of the ALHAMBRA optical photometric system, we refer the reader to Cristóbal-Hornillos et al. (in preparation).

The ALHAMBRA survey has used the Two-Micron All-Sky Survey (2MASS) catalogue (Cutri et al. 2003) to calibrate its NIR images. As explained in Cristóbal-Hornillos et al. (2009), several dozens of stars common to both data sets with high S/N were selected in each field, yielding photometric zero-point offsets with uncertainties of ∼0.03 mag. We will discuss the procedure to refine

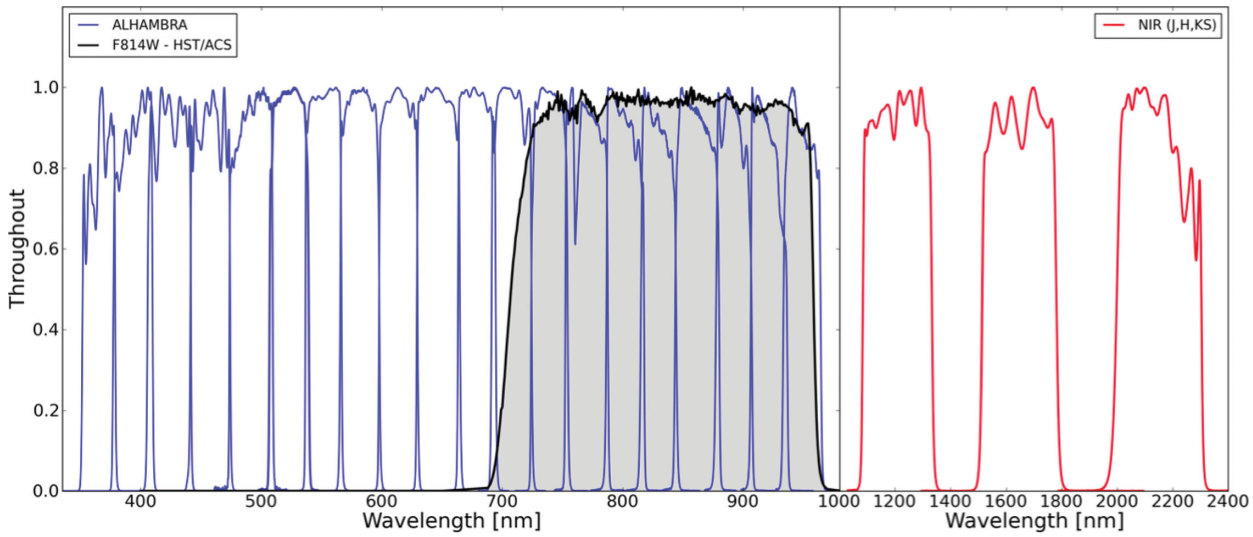

Figure 2. The ALHAMBRA survey filter set. On the left-hand side, solid blue lines represent the optical filter system composed of 20 contiguous, equal-width, non-overlapping, medium-band (∼300 Å) filters. The solid black line corresponds to the synthetic *F*814*W* filter used to define a constant observational window across fields. On the right-hand side, solid red lines represent the standard *JHKs* near-infrared broad bands. All transmission curves are normalized to the maximum value.

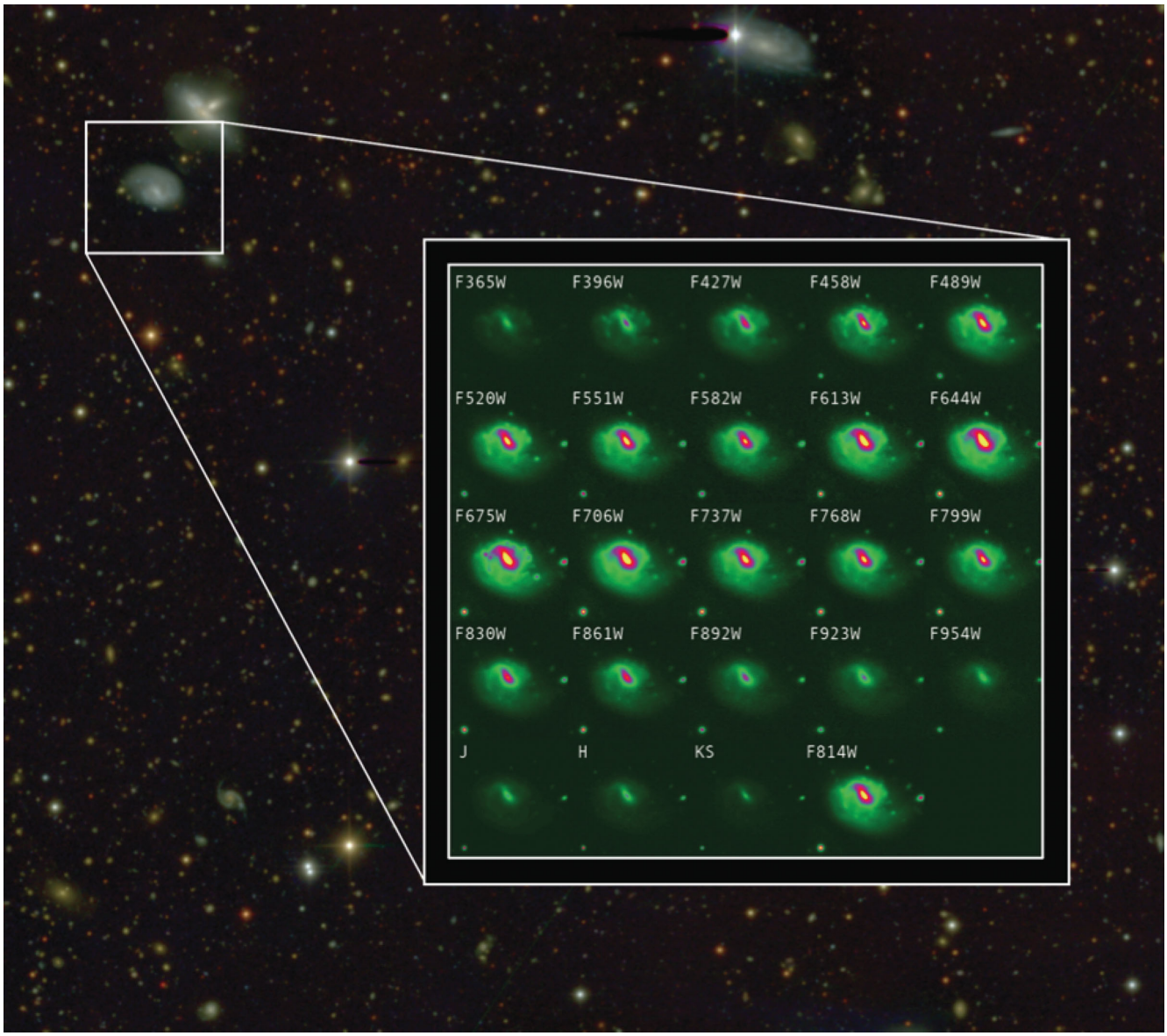

Figure 3. The ALHAMBRA survey. The figures show how a galaxy looks when observed through the ALHAMBRA filter system. The optical range is covered horizontally from top to bottom and left to right; the last row corresponds to the *J*, *H* and *Ks* NIR filters, along with the synthetic *F*814*W* detection image. The background colour image was generated using the TRILOGY software (http://www-int.stsci.edu/ dcoe/trilogy/Intro.html).

the photometric zero-point calibrations via SED-fitting techniques in Section 4.2.1.

3 PHOTOMETRY

3.1 Multi-wavelength photometry

As was thoroughly described in Coe et al. (2006), measuring multicolour photometry in images with different PSFs is not a trivial task. To perform good quality multicolour photometry, it is necessary to sample the same physical region of the galaxy taking into account the smearing produced by different PSFs, as seen in Fig. 4. We show the distribution of optical, NIR and synthetic *F*814*W* PSFs in the ALHAMBRA survey in Fig. 5, for values between 0.7 and 1.6 arcsec.

One of the methods to correct for PSF effects is to smooth the whole data set to the worst seeing condition, making all images look as they had been taken under the same seeing conditions (Loh & Spillar 1986; Labbé et al. 2003; Capak et al. 2007). This methodology produces consistent apertures across the filters, but strongly degrades the best observations to the level of the worst. Here we have used ColorPro (Coe et al. 2006), which corrects accurately for PSF effects without degrading image quality; Laidler et al. (2006), de Santis et al. (2007), Kuijken (2008) and Wolf et al. (2008) have also developed similar approaches.

To improve the photometric depth and homogeneity, we relied on deep synthetic *F*814*W* images (Section 3.5), which are the best option for photometric aperture definitions (given the enhanced S/N) and galaxy morphology estimations.

3.2 PSF-matched aperture-corrected photometry

ColorPro derives accurate PSF-corrected photometry without degrading high-quality images. Initially the software defines every

Table 3. Summary of the multiwavelength filter set for ALHAMBRA. The full width at half-maximum (FWHM), exposure time and limiting magnitude (measured using a 3-arcsec diameter aperture) correspond to the average value among the 48 CCDs.

Camera	Filter	$\lambda_{\rm eff}$ [Å]	FWHM [Å]	$\langle t_{\rm exp}\rangle$ [s]	$\langle m_{\rm lim}^{(3'')}\rangle$ (5σ)
Optical					
LAICA	F365W	365	279	3918	23.7
LAICA	F396W	396	330	2896	23.8
LAICA	F427W	427	342	2774	23.8
LAICA	F458W	458	332	3079	23.8
LAICA	F489W	489	356	2904	24.2
LAICA	F520W	520	326	2664	24.1
LAICA	F551W	551	297	2687	23.7
LAICA	F582W	582	324	2936	23.8
LAICA	F613W	613	320	2940	23.9
LAICA	F644W	644	357	4043	23.8
LAICA	F675W	675	314	4575	23.5
LAICA	F706W	706	332	5668	23.7
LAICA	F737W	737	304	7095	23.5
LAICA	F768W	768	354	8824	23.5
LAICA	F799W	799	312	8992	23.2
LAICA	F830W	830	296	11 436	23.2
LAICA	F861W	861	369	10 505	22.9
LAICA	F892W	892	303	9044	22.5
LAICA	F923W	923	308	6338	22.1
LAICA	F954W	954	319	5620	21.5
NIR					
OMEGA	*J*	1216	2163	5169	22.6
OMEGA	*H*	1655	2191	5055	21.9
OMEGA	*Ks*	2146	2412	5050	21.4
Detection					
SYNTH	*F*814*W*	845	2366	73 522	24.5

photometric aperture based on the selected detection image. Then it goes filter by filter and estimates how much flux a galaxy has missed within that aperture as a consequence of the difference between the PSF of the image in that filter and the detection PSF. This correction is applied to each filter, yielding PSF-corrected magnitudes with as little PSF degradation as possible.

SExtractor (Bertin & Arnouts 1996) ISOphotal apertures produce the most robust colours for faint objects (Benítez et al. 2004), while SExtractor AUTO apertures provide better estimations of galaxy total magnitudes. To encompass the usefulness of both measurements, ColorPro defines a photometric transformation that provides both SExtractor ISOphotal colours and total magnitudes.

Total magnitudes are defined as

$$M_i = M_i^{\rm ISO} + \left(M_{\rm det}^{\rm AUTO} - M_{{\rm det},i}^{\rm ISO}\right), \quad (1)$$

where the first term corresponds to the standard SExtractor ISOphotal magnitude for sources detected in the *i*th band, while the second term incorporates the PSF correction (by applying the photometric differences when degrading the detection image ($M_{\rm det}$) to the *i*th-PSF condition ($M_{{\rm det},i}$)). Hence, the second term extends SExtractor ISOphotal magnitudes into total magnitudes.

Meanwhile, ISOphotal colours are derived as

$$M_j = M_j^{\rm ISO} + \left(M_{\rm det}^{\rm AUTO} - M_{{\rm det},j}^{\rm ISO}\right), \quad (2)$$

$$M_i - M_j = M_i^{\rm ISO} - M_j^{\rm ISO} + \left(M_{{\rm det},j}^{\rm ISO} - M_{{\rm det},i}^{\rm ISO}\right), \quad (3)$$

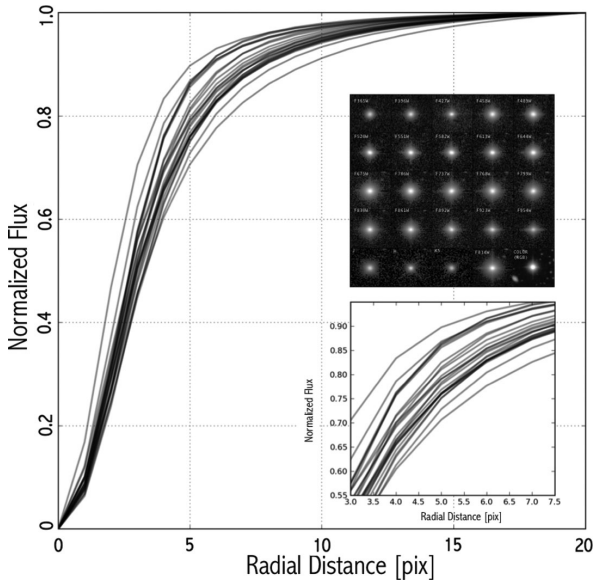

Figure 4. Seeing variability across photometric bands. For a single star, solid black lines represent the scatter in the normalized stellar growth curve as a consequence of the varying PSF across filters (inset top panel). This effect has to be corrected in order to estimate accurate colours.

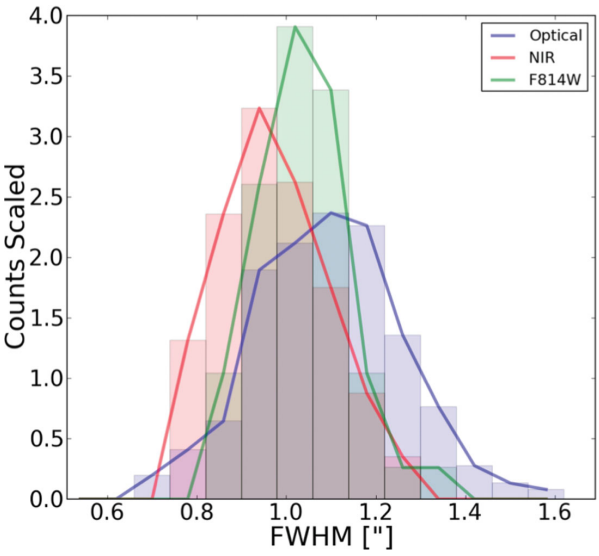

Figure 5. Distribution of seeing conditions for the ALHAMBRA fields. The figure shows the distribution of PSFs (measured as the FWHM in arcsec) for optical images (blue), NIR (red) and synthetic *F*814*W* detection images (green). The PSFs range from 0.7–1.6 arcsec, with the optical images having $\langle$FWHM$\rangle \sim 1.1$ arcsec, NIR images $\langle$FWHM$\rangle \sim 0.9$ arcsec and synthetic *F*814*W* detection images $\langle$FWHM$\rangle \sim 1.0$ arcsec.

where resulting $M_i - M_j$ colours are just the combination of their SExtractor ISOphotal magnitudes plus a second term including their relative PSF corrections. As expected, in those cases with equal PSF the second term might be cancelled out, providing colours directly from the SExtractor ISOphotal magnitudes. For a more detailed explanation, we refer the reader to Coe et al. (2006).

3.3 PSF models

As required by ColorPro, it was necessary to generate PSF models for each individual image. We used the package daophot from

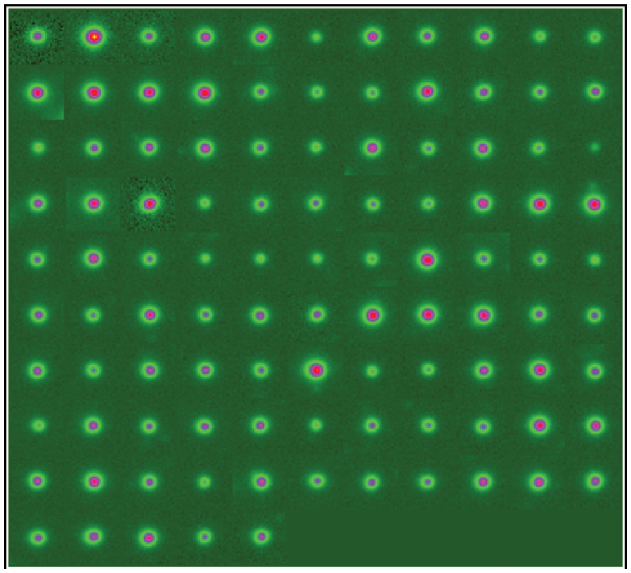

Figure 6. Star selection. Several hundred non-saturated and well-isolated stars were interactively selected across the images, to derive the PSF models. A careful selection is essential to ensure the accuracy of the PSF-corrected magnitudes.

IRAF (Stetson 1987), which uses a hybrid method to compute PSF models. It first fits the central region of the stars by using an analytical function (Gaussian, Lorentzian, Moffat or Penny) and then the outermost parts (regions connected with the background) are empirically fitted point by point; typical residuals between stars and models are around ∼3 per cent.

We initially ran SExtractor on each image using a very high threshold ($\sim 100 \times \sigma_{\rm Background}$) to detect only bright sources. We kept detections with SExtractor *CLASS_STAR* > 0.9. When plotting the magnitude versus the full width at half-maximum (FWHM) for those selected objects, we find that they are located in the region of the brightest and most compact sources (Section 3.6.1). To avoid both saturated stars and misclassified galaxies, we culled objects outside the range $16 < m < 22.5$, yielding a final sample of several hundred stars per image.

Afterwards, we visually rejected stars with contaminating neighbours and generated mosaic-like images (Fig. 6). These images decreased the computational time required by DAOPHOT to model the PSF and generated much higher quality results. Finally, the PSF models were normalized to the same flux. Among the different analytical models considered by DAOPHOT, the most recurrent one was the Penny2 profile. This model consists of a Gaussian-like function but with Lorentzian wings. Although typical residuals for PSF models from CCD1, CCD2 and CCD4 are around 3 per cent, CCD3 shows a different behaviour, with systematically larger residuals of 5–10 per cent. This different behaviour was probably due to the differences in the efficiency of this detector (CCD3), which was not science grade and was significantly worse than CCD1, CCD2 and CCD4 (Cristobal-Hornillos et al., in preparation).

3.3.1 PSF model verification

We systematically verified each PSF model. First, we compared its FWHM with the registered seeing (from the image header) and with the mean FWHM value for the stars used to derive the model. The observed scatter among PSFs does not exceed 3–5 per cent, ensuring that stars and models are well in agreement.

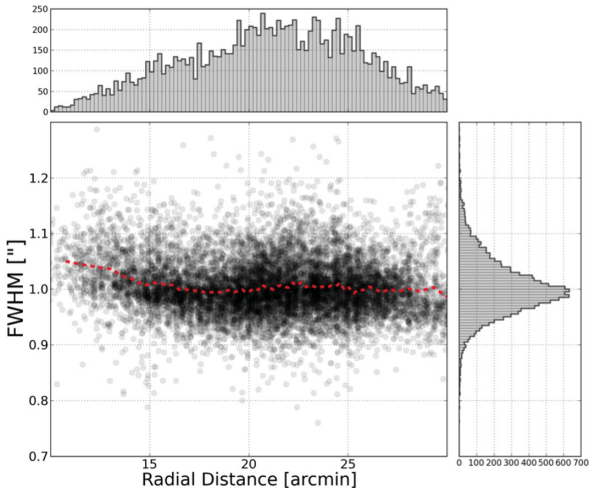

Figure 7. Radial PSF variability across images. The figure shows the radial dependence of the PSF (expressed in arcsec and referred to the primary mirror telescope) for the compilation of stars used to derive the PSF models. The mean value of the distribution (dashed red line) has a scatter smaller than 5 per cent, enabling the usage of a single PSF model per image.

The PSF stability among different CCDs was also checked. As introduced in Section 2.2, given the spatial configuration of the LAICA optical system, the four CCDs simultaneously imaged similar parts of the sky under the same atmospheric conditions and with the same passbands. This fact made it possible to perform statistical comparisons among detectors. Once again we observed good agreements among CCD1, CCD2 and CCD4, but a larger deviation for CCD3 close to 5–10 per cent.

Finally, we studied the radial PSF variability across images to ascertain the usage of a single PSF model per image. We defined a new reference system linking every detection (from each CCD) to the centre of the telescope's focal plane. In Fig. 7, we show the dependence of the FWHM as a function of the radial distance for ∼20 000 stars, finding a variation smaller than 5 per cent.

3.4 Simulations

We carried out several simulations to test the accuracy of ColorPro. To do so, we degraded a much better resolution image to the typical ALHAMBRA conditions (in terms of PSF and background noise) and ran ColorPro on it, expecting to retrieve null colours (equal magnitudes) for galaxies observed under different PSFs.

We created a mosaic image by rearranging four *HST*/ACS *F*814*W* images from the COSMOS survey (Scoville et al. 2007) that overlap the ALHAMBRA fields. We rescaled the mosaic to the ALHAMBRA pixel size (from the ACS 0.065 arcsec pixel^{-1} to the LAICA 0.221 arcsec pixel^{-1}), convolved with ∼200 PSFs randomly drawn from our models and reapplied background noise using typical values for the ALHAMBRA images (empirically measured as explained in Section 3.7). An example of the simulated images is shown in Fig. 8, which compares the *HST*/ACS image of a galaxy (left panel) with the ALHAMBRA image (middle panel) and the simulated image (right panel).

3.4.1 Reliability

We ran ColorPro on the new set of ∼200 mosaics, using the same configuration used for the ALHAMBRA catalogues. We excluded

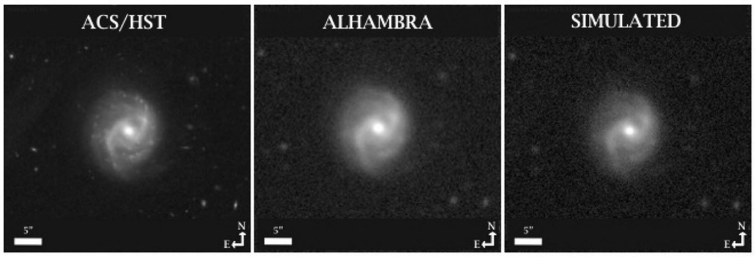

Figure 8. Example of the simulated data set reproducing the typical observational conditions of the ALHAMBRA images (Section 3.4). From left to right, we show a galaxy in the ACS/*HST* image, ALHAMBRA synthetic *F*814*W* detection image and rescaled + PSF degraded + background reapplied ACS/*HST* image.

all detections with photometric problems reported by SExtractor (SExtractor_*Flag*>1) to eliminate several ghosts and other artefacts (trails) within the original images.

We found that the simulated colours showed a dispersion of $\sigma \sim 0.03$, which marks a photometric precision floor, for sources brighter than magnitude $m_{F814W} = 23.0$ and, as expected from the uncertainties arising from the photometric noise, an increasing error for fainter magnitudes. For most of the magnitude range there are negligible biases, as seen in the top panel of Fig. 9. This shows that ColorPro is capable of performing accurate PSF corrections for ALHAMBRA-like data.

3.4.2 *Completeness*

We studied the expected photometric completeness for the ALHAMBRA fields in terms of PSF and background level. For this purpose, we used the previous simulations to derive the statistical probability of detecting a sample of faint galaxies when observed under typical ALHAMBRA conditions. In the bottom panel of Fig. 9 we show the expected fraction of missed galaxies per magnitude range and square degree. The result indicates that ALHAMBRA is photometrically complete down to a magnitude of $m_{F814W} \sim 24$. At fainter magnitudes, the number of detections decreases rapidly, with ∼40 per cent of the galaxies lost at $m_{F814W} \sim 25$.

3.5 Synthetic *F*814*W* detection images

In photometric surveys it is a common practice to stack the best quality images in order to generate detection images that are deeper than the images obtained in any individual filter. To define a homogeneous detection image for all ALHAMBRA fields, we generated synthetic *F*814*W* images as the properly weighted combination of several individual bands. To calculate the weights we generated, using the empirically calibrated template library of Benítez (2014), a realistic galaxy mock catalogue up to the typical ALHAMBRA depth and solved using least-squares, the system of equations between the corresponding synthetic colours (equation 4).

The system of equations between filters for N_g galaxies is defined as follows:

$$m_{F814W,i} = \sum_{j=1}^{N_f} a_{i,j} \times m_{i,j}. \quad (4)$$

An example of the so-derived synthetic *F*814*W* images is shown in Fig. 10. The least-squares solution, with an rms error smaller

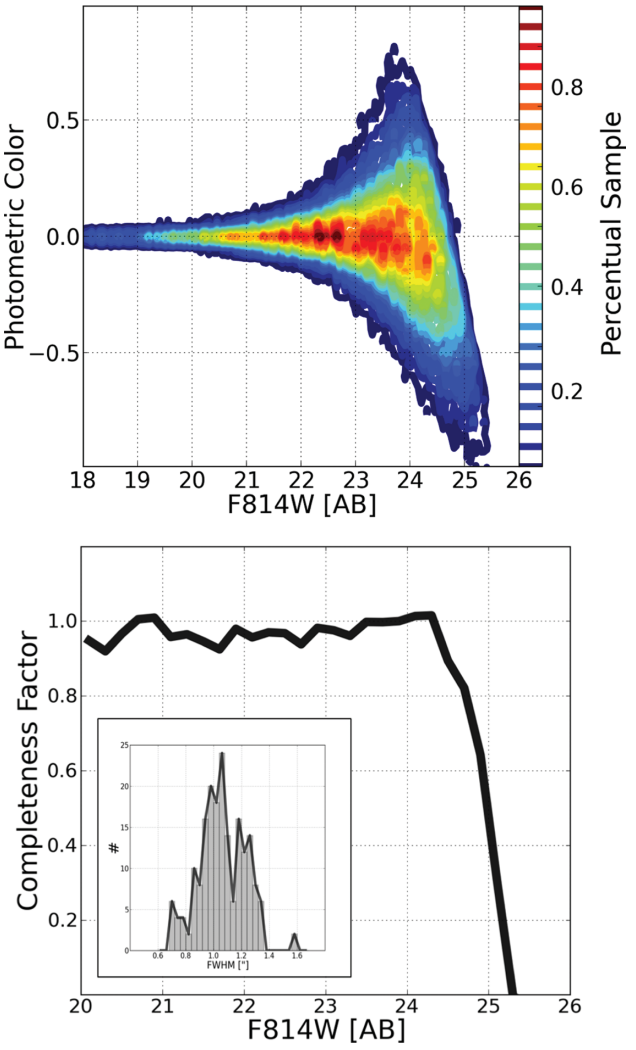

Figure 9. PSF-corrected photometry verifications. We designed a set of simulations (Section 3.4) to estimate both the reliability of ColorPro in deriving PSF-corrected photometry and the expected completeness in our images. The top panel shows how ColorPro successfully retrieved null colours (same magnitudes) across simulated images, with a dispersion below 3 per cent for magnitudes brighter than $m_{F814W} = 23.0$ and an increasing error, as expected from the added photometric noise, at fainter magnitudes. The bottom panel shows the expected completeness as a function of *F*814*W* magnitude.

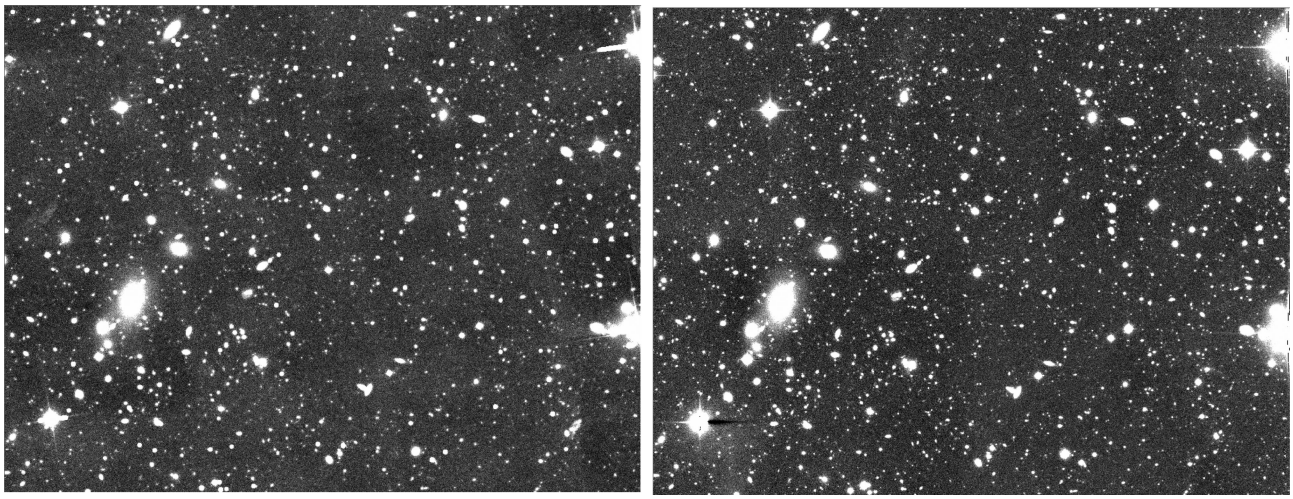

Figure 10. Example of the synthetic *F*814*W* images derived for the ALHAMBRA fields. The left panel shows how the original *HST*/ACS *F*814*W* image looks after being scaled to the ALHAMBRA pixel size, convolved with the ALHAMBRA PSF and with photometric noise reapplied. The right panel shows the synthetic ALHAMBRA *F*814*W* detection image.

than 1 per cent, is

$$
\begin{aligned}
F814W = \\
&0.105 \times \mathbf{F706W} + 0.178 \times \mathbf{F737W} + 0.179 \times \mathbf{F768W} \\
&+ 0.142 \times \mathbf{F799W} + 0.115 \times \mathbf{F830W} + 0.119 \times \mathbf{F861W} \\
&+ 0.073 \times \mathbf{F892W} + 0.049 \times \mathbf{F923W} + 0.040 \times \mathbf{F954W}. \qquad (5)
\end{aligned}
$$

Given that the typical error in the individual bands is 2–3 per cent, total zero-point error in the *F*814*W* image is quite small, providing high homogeneity. To verify the calibration of the synthetic *F*814*W* images, we performed a photometric comparison with the COSMOS field. To reproduce the same photometric measurements as in Ilbert et al. (2009), we ran SExtractor using fixed circular apertures of 3 arcsec. We retrieved ∼10 800 common sources with ALHAMBRA in the $19 < m_{F814W} < 25.5$ range. The photometric comparison is shown in Fig. 11.

No photometric zero-point offsets or trends are apparent up to magnitudes $m_{F814W} = 23.5$. For the faintest sample, the retrieved photometric colour (COSMOS/*F*814*W* magnitude − ALHAMBRA/*F*814*W* magnitude) becomes progressively negative, indicating that COSMOS magnitudes are brighter than ALHAMBRA's. The trend observed seems to be caused by a combination of an aperture and filter shape effect. On the one hand, as explained in Section 3.3, the ALHAMBRA PSF models seemed to prefer a Penny2 profile, which consists of a Gaussian-like function but with Lorentzian wings; in addition, the PSF is almost an order of magnitude larger than the PSF. This much more extended PSF spreads flux outside the aperture diameter, an effect that is much more important for the faintest sources. This is also observed in the simulation in Section 3.4. In Fig. 9 (top panel), the same trend is observed at faint magnitudes. On the other hand, the ALHAMBRA/*F*814*W* images were created combining the last optical individual filters as shown in equation (5). Unfortunately, the last *F*892*W*, *F*923*W* and *F*954*W* optical filters have relatively low S/N. Therefore our '*F*184' filter becomes progressively bluer with magnitude, thus having a much wider PSF, which intensifies the above-described effect.

In an effort to extend the accuracy of the ALHAMBRA photometric measurements, we derived a magnitude-dependent correction to make ALHAMBRA magnitudes reproduce the COSMOS estimations for fixed apertures of 3 arcsec. These corrected magnitudes are included in the final catalogues, as explained in Appendix C.

We also ran SExtractor on both ACS/*F*814*W* and synthetic ALHAMBRA/*F*814*W* images using the same SExtractor configuration. This analysis provided a characterization of the differences in the detections between both images. For detection magnitudes $19 < m_{F814W} < 23.5$, only a few dozen sources per CCD were missing from the synthetic ALHAMBRA/*F*814*W* images. Detections fainter than magnitudes $m_{F814W} = 23.5$ showed an increasing distribution of undetected sources peaking at a magnitude $m_{F814W} \sim 25.5$, well beyond the ALHAMBRA photometric completeness limit.

3.5.1 *Masks*

In order to improve the source detection efficiency, we masked every saturated star, stellar spike, ghost and damaged area. Initially we ran SExtractor on each synthetic *F*814*W* detection image with a special configuration to detect just very bright and extended sources. We visually checked the extracted sources to exclude any possible nearby galaxy. Then we convolved the resulting SExtractor segmentation maps with a Gaussian function to broaden the previously defined apertures and so remove residual contributions from stellar haloes. We repeated the same procedure on the inverse image to deal with negative extended regions generated by saturated stars. We combined both positive and negative segmentation maps, defining the total region to be masked out. Finally, we replaced all flagged pixels with background noise to minimize the variation of the image root-mean-square error (RMS). An example of the masking procedure for a saturated star is shown in Fig. 12.

3.5.2 *SExtractor configuration*

Assuming an expected variability in terms of PSF (and therefore in photometric depth) among the *F*814*W* detection images, we explored the optimal SExtractor configuration that maximizes the number of real detections. For non-crowded fields, the most relevant parameters are the minimum number of contiguous pixels *DETECT_MINAREA* and the threshold the signal has to exceed to be considered a real detection *DETECT_THRESHOLD*.

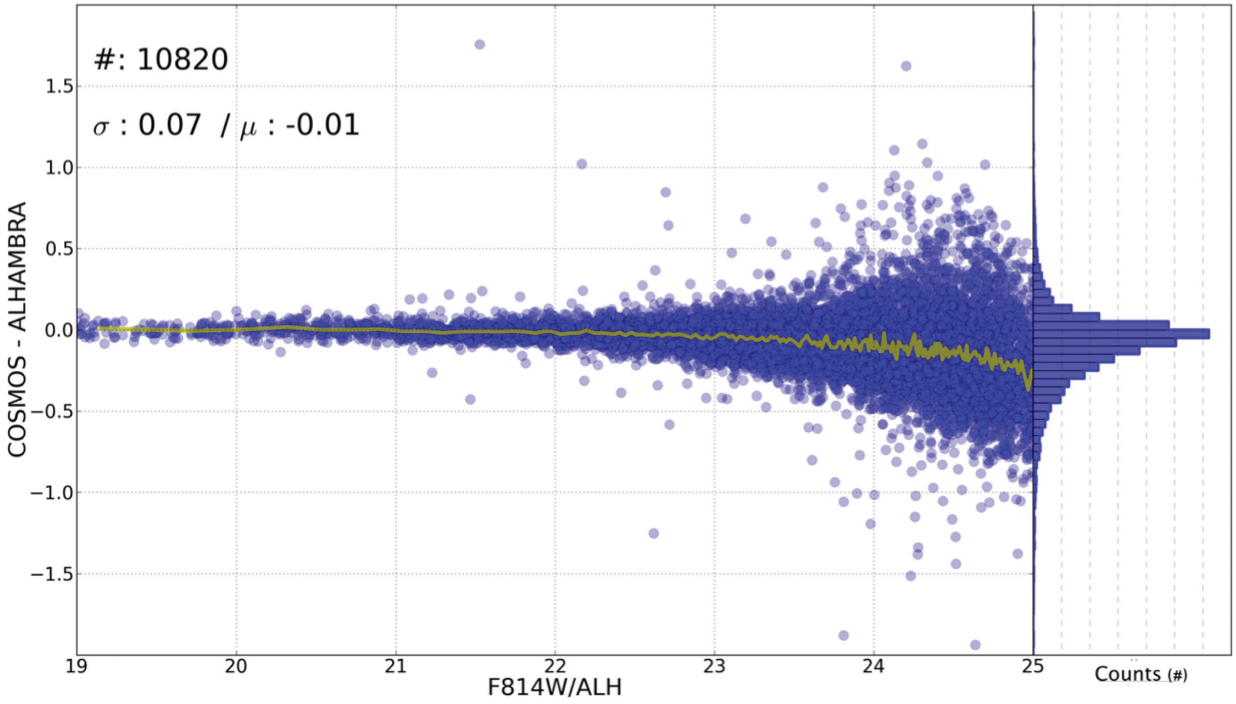

Figure 11. Photometric comparison between the *F*814*W*/COSMOS and synthetic ALHAMBRA/*F*814*W* images. In order to reproduce the same photometric measurements as Ilbert et al (2009), we ran SExtractor on the synthetic ALHAMBRA/*F*814*W* images using fixed circular apertures of 3 arcsec. Selecting a common sample of ∼10 800 detections between ALHAMBRA and COSMOS, we found neither photometric zero-point offsets nor significant bias for detections with magnitudes $19 < m_{F814W} < 23$. For sources fainter than $m_{F814W} = 23.0$, an increasing dependence on the magnitude is observed as a consequence of the rapidly decreasing S/N for the ALHAMBRA detections. To match the ALHAMBRA and COSMOS *F*814*W* magnitudes for fixed 3-arcsec apertures, we derived a magnitude-dependent correction that is included in the final catalogues, as explained in Section 5.

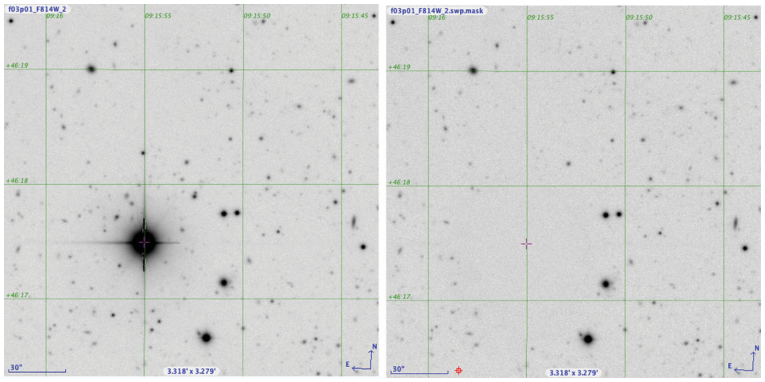

Figure 12. Star masking. In order to improve both the photometric depth and the photometric measurements, *F*814*W* detection images were masked out, purging saturated stars, spikes, ghosts, negative areas and other artefacts. This figure shows an example of how a saturated star from the original image (left panel) disappears after replacing all its pixels with background signal (right panel).

In the Gaussian limit, the sky noise should in principle have a symmetric structure and a similar amount of spurious objects are expected to be found on both sides of the image. Using this assumption, we looked for the SExtractor detection threshold that produced no more than 3 per cent contamination by spurious detections. We fixed *DETECT_MINAREA* at twice the image FWHM and ran SExtractor on both the image and its inverted negative side. The results are shown in Fig. 13. In the Appendix D, we show an example of the typical configuration used to perform source detection.

3.5.3 Flag images

In order to be able to quantify the survey effective area, we generated FLAG images for each individual CCD where all problematic pixels were set to 0. As the effective exposure time rapidly decreases when approaching the image edges, we defined homogeneous areas where all sources have adequate exposure in all the 23 bands. We normalized individual weight maps to the maximum exposure time and then flagged the regions with a relative exposure time below 60 per cent (mostly near the image edges).

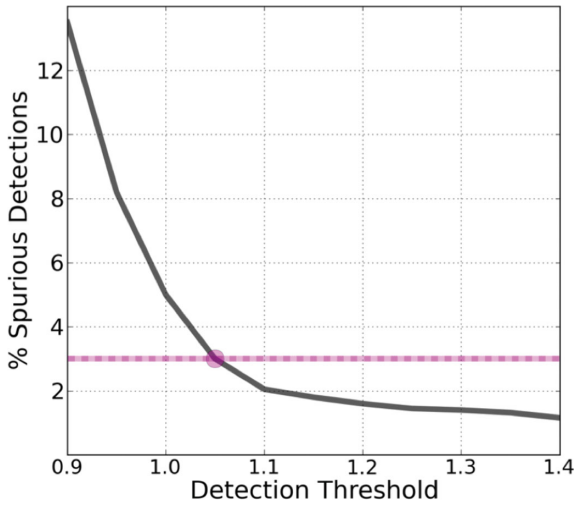

Figure 13. Detection threshold. We fixed *DETECT_MINAREA* at twice the image FWHM and then ran SExtractor on the positive and inverted negative image, obtaining the fraction of spurious over real detections as a function of *DETECT_THRESHOLD*. We set the threshold to the value that reported no more than 3 per cent spurious detections.

The flag images also incorporate the stellar mask information (Section 3.5.1); masked out regions are replaced by background noise in the science images, to avoid interfering with SExtractor background determination. We compute the effective area for each $F814W$ detection image as the direct conversion of the total number of non-flagged pixels into deg^2, as shown in Table D2. Including all 48 $F814W$ detection images yields a total surveyed area of 2.79 deg^2.

3.5.4 RMS images

As the effective exposure time on an image is position-dependent, detected sources at the edges will have shorter exposures than sources in the centre, generating S/N gradients. From a source-detection point of view, as synthetic $F814W$ images are generated as the combination of many filters, occasional inhomogeneities registered on individual WEIGHT maps become averaged out. However, on individual filters (especially for the case of NIR images) we found occasional inhomogeneities across the images (Cristóbal-Hornillos, in preparation), which affects the photometric depth.

To help disentangle whether a galaxy may be missed in a given filter as a consequence of its intrinsic luminosity (below the detection threshold) or due to an insufficient photometric depth, we used the WEIGHT maps (Cristóbal-Hornillos, in preparation) to generate a new set of inverse RMS images and define two additional photometric flags using the following expression:

$$1/RMS = \sqrt{Weight}. \quad (6)$$

Hence, the *irms_OPT_Flag* and *irms_NIR_Flag* flags indicate the number of individual bands in which an object has a signal in its inverse RMS below 80 per cent of the maximum value. Therefore, galaxies with large values in these photometric flags (indicating a large fraction of filters photometrically flagged) may provide unreliable photometric redshift estimations.

3.6 Star/galaxy separation

The star/galaxy classification is a necessary step for accurate extragalactic surveys. Stars as real point-like sources (PLS) are observed as the most compact objects in an astronomical image. However, as objects get fainter (decreasing the S/N) it becomes progressively harder to discern their real morphologies.

We followed a statistical approach to perform star/galaxy separation. We assigned a probability to every detection given its apparent geometry, $F814W$ magnitude, optical $F489W - F814W$ and NIR $J - Ks$ colours. For each variable, we derived the corresponding probability distribution function (PDF) based on the typical distribution of stars and galaxies. Therefore, every detection is classified in terms of the probability of being a star or a galaxy, as follows:

$$P_{\rm Star} = P_{\rm Star}^{\rm FWHM} \times P_{\rm Star}^{m_{F814W}} \times P_{\rm Star}^{\rm Opt} \times P_{\rm Star}^{\rm NIR}, \quad (7)$$

$$P_{\rm Gal} = P_{\rm Gal}^{\rm FWHM} \times P_{\rm Gal}^{m_{F814W}} \times P_{\rm Gal}^{\rm Opt} \times P_{\rm Gal}^{\rm NIR}, \quad (8)$$

where

$$P = P_{\rm Star} + P_{\rm Gal} = 1. \quad (9)$$

Final probabilities are stored in the statistical variable *Stellar_Flag* included in the catalogues. The derivation of each of the four independent PDFs is described below.

3.6.1 Geometry and magnitude

We used the COSMOS *HST*/ACS images to explore the star/galaxy selection algorithms, since they are considerably deeper and with an obviously much narrower PSF than the ALHAMBRA data set.

We ran SExtractor twice, first on the ACS/$F814W$ images and then on the ALHAMBRA/$F814W$ images in single-image mode, plotting the detected sources in a FWHM versus $m_{\rm ACS/F814W}$ diagram as shown in Fig. 14. We selected detections classified as PLS (point-like sources) in the ACS/$F814W$ images and used them to match the ALHAMBRA/$F814W$ detections.

As seen in Fig. 14, sources brighter than $m_{\rm ACS/F814W} = 22.5$, classified as PLS on the ACS/$F814W$ images, were equally classified as PLS on the ALHAMBRA/$F814W$ (open red circles). However, PLS fainter than $m_{\rm ACS/F814W} = 22.5$ showed progressively larger FWHM values in the ALHAMBRA/$F814W$ images. Therefore, ALHAMBRA images cannot be used reliably for morphological information fainter than $m_{F814W} = 22.5$.

We also investigated the nature of the faint detections appearing as PLS in the ALHAMBRA/$F814W$ images but clearly not belonging to the ACS/$F814W$ PLS sample (green dots). We inverted the procedure, selecting faint $m_{F814W} > 22.5$ PLS in ALHAMBRA and matching them to the ACS/$F814W$ detections. The result showed that some of those detections were actually very faint extended sources in the ACS images and were classified as PLS in the ALHAMBRA/$F814W$ images because only the central, compact region of the source was detected above the detection threshold.

3.6.2 Photometric colours

Stars can be told apart from galaxies based on their spectral differences (Daddi et al. 2004). By combining two photometric colours (one in the optical, one in the NIR), it is possible to identify two separated regions where stars and galaxies are typically located, as shown in the left panel of Fig. 15. We use the optical $F489W - F814W$ and NIR $J - K_s$ to study how well the colour–colour method works with increasing photometric depth in the ALHAMBRA images.

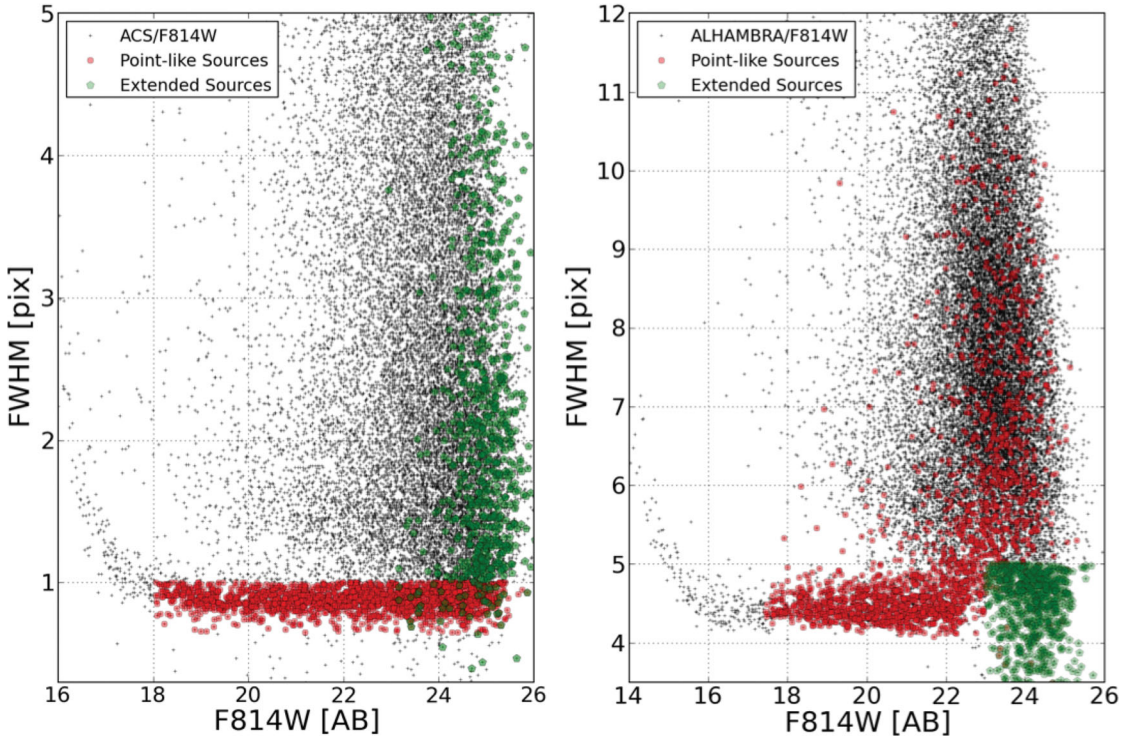

Figure 14. We studied the shape degradation of point-like sources observed in our fields as a function of the apparent magnitude. We used the ACS/*F*814*W* images from COSMOS to select real point-like sources (narrowest FWHM) within the ALHAMBRA fields and so understand what these sources might look like when observed under ALHAMBRA PSF conditions. As can be seen in the figure, $m_{\mathrm{ACS/F814W}} < 22.5$ objects classified as point-like sources in the ACS/*F*814*W* images (red circles) were also classified as point-like sources on the ALHAMBRA/*F*814*W* images. However, point-like sources on the ACS/*F*814*W* images with $m_{\mathrm{ACS/F814W}} > 22.5$ show an increasingly wider FWHM in the ALHAMBRA/*F*814*W* images. This fact illustrates the degradation of purely 'geometrical' information with decreasing S/N. Inverting the procedure, we also find that point-like sources in the ALHAMBRA images below the m_{F814W} threshold are often the central regions of extended, faint objects in the ACS images.

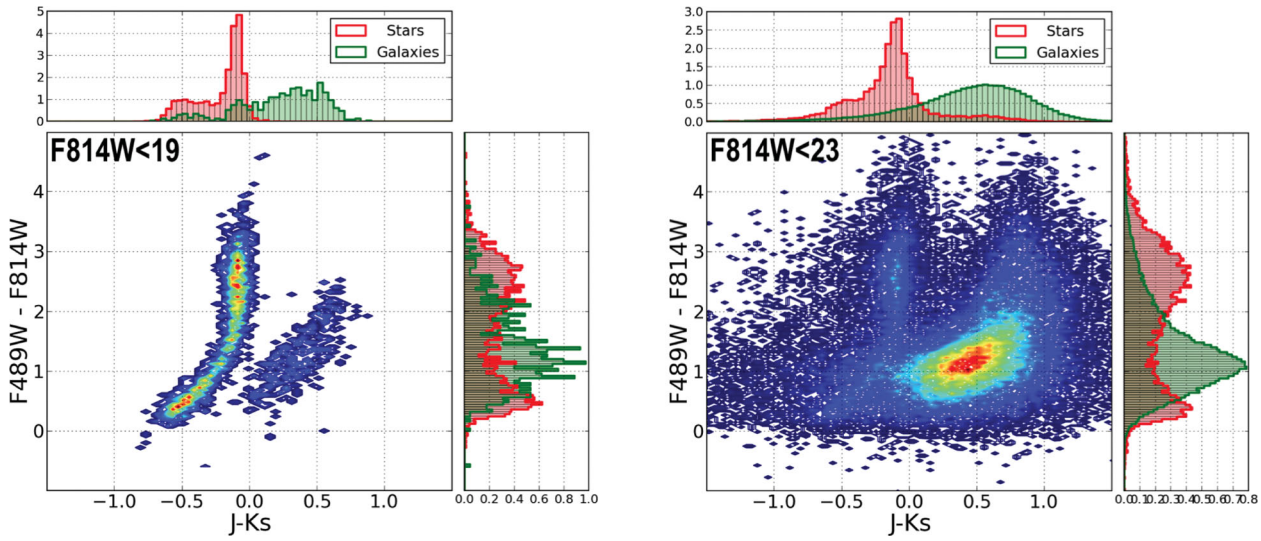

Figure 15. Effect of photometric uncertainties on the separation between stars and galaxies. The $F489W - F814W/J - K_S$ colours of objects classified as point-like sources in the ACS/*F*814*W* images are plotted on the left, those of extended objects on the right. This diagram is a very useful discriminating tool for $m_{F814W} < 22.5$ but becomes almost useless at fainter magnitudes.

In order to generate a control sample, we assumed that real PLS (as classified by ACS/*F*814*W* images) were all 'stars', whereas well extended sources (ES) were assumed to be 'galaxies'. Considering the resolution of the ACS/*HST* images and the magnitude range involved in this analysis, the sample of stars/galaxies derived represented a good approximation, as the expected fraction of misclassified galaxies or quasi-stellar objects (QSOs) is actually negligible.

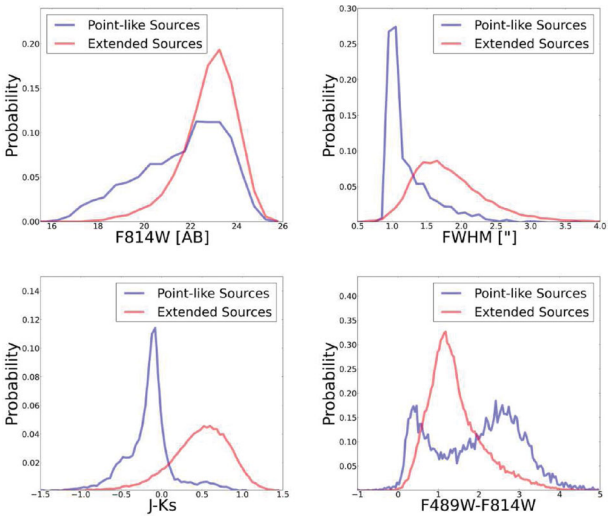

Figure 16. Star/galaxy PDFs. The figure shows the four PDFs derived for a control sample of stars and galaxies selected from the ACS/*F*814*W* images. From left to right and top to bottom, the distribution of stars (blue line) and galaxies (red line) is shown as a function of the apparent magnitude *F*814*W*, apparent FWHM, NIR and optical colours. These PDFs were used to estimate the probability of a detection being a star or a galaxy, as explained in Section 3.6.3.

We tested the reliability of this methodology by gradually decreasing the S/N of the sample. Initially, we selected only sources with very high S/N ($m_{F814W} < 19$), as shown in the left-hand side of Fig. 15. However, as sources get fainter ($m_{F814W} < 23$, on the right-hand side), separating the two classes becomes progressively complicated, with ES and PLS spreading into the stellar and galactic loci respectively.

3.6.3 *Stellar flag*

Finally, we used the retrieved information from the star/galaxy geometry, *F*814*W* magnitude, optical and NIR colours to derive empirical PDFs as shown in Fig. 16. Therefore we assigned a statistical classification to every detection given its observed information. Considering the level of both photometric and geometric uncertainties when deriving the PDFs, we excluded from the classification all detections with $m_{F814W} > 22.5$, assigning them a *Stellar_Flag* value = 0.5.

We tested the goodness of this statistical classification by comparing the density of selected stars per unit of area with the numbers expected from the model of Girardi et al. (2002, 2005), implemented in the TRILEGAL software, as a function of the area, galactic position and limiting magnitude. As seen in Fig. 17, we find very good agreement between measurements and predictions; this is optimized by using a threshold of Stellar_Flag > 0.7 to select our stars.

As shown in the right panel of Fig 17, when applying this criterion, we observe that stars dominate the sample down to a magnitude $m_{F814W} < 19$. For fainter magnitudes, the fraction of stars declines rapidly, with a contribution of ∼10 per cent for magnitudes $m_{F814W} = 22.5$. As indicated in the inset panel, if we extrapolate the stellar number counts thus derived, the expected contamination for unclassified stars with magnitudes fainter than $m_{F814W} > 22.5$ becomes negligible, with a contribution of stars of ∼1 per cent for magnitudes $m_{F814W} = 23.5$. We retrieve an averaged stellar density in the galactic halo of ∼7000 stars per deg^2 (∼450 stars per CCD) for sources brighter than $m_{F814W} = 22.5$.

3.7 Photometric errors

Many of the steps involved in image processing introduce correlations between neighbouring pixels, making the background noise in images different from a Poissonian distribution. If these effects are not properly taken into account, they can lead to a severe

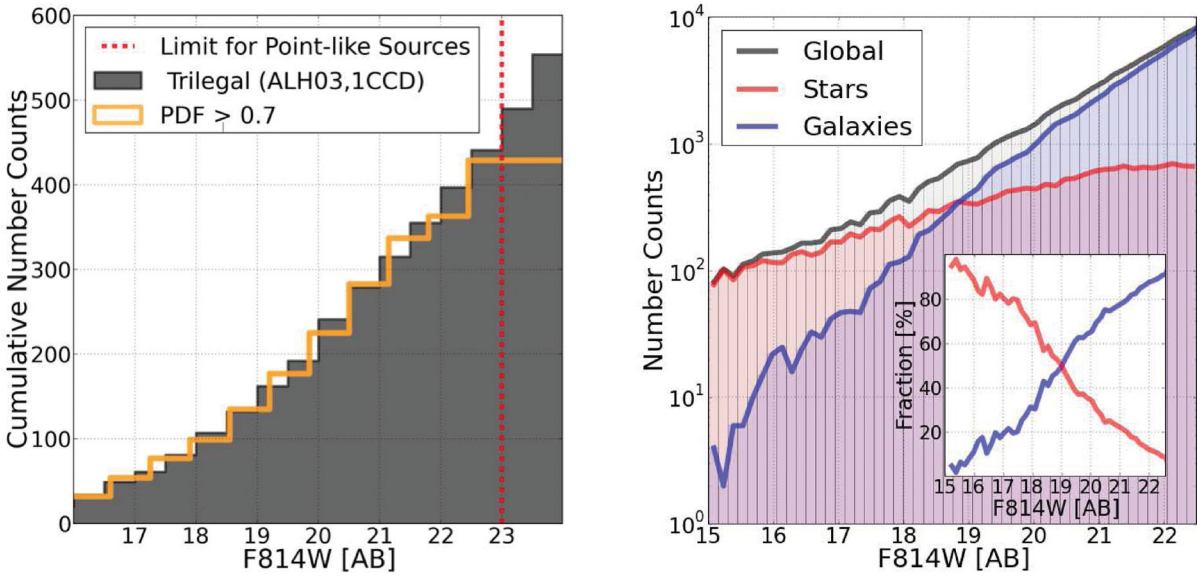

Figure 17. Star number counts. For each field in ALHAMBRA, we compared the number of detections classified as stars based on our statistical criteria (solid yellow line) with that provided by the TRILEGAL software (solid grey histogram), as seen in the left panel. The figure shows an example for a single CCD in the ALHAMBRA-03 field. The best match is reached for *Stellar_Flag* > 0.7. When applying this statistical criterion to the whole catalogue (right panel), we observe stars to dominate the sample down to a magnitude $m_{F814W} < 19$. At fainter magnitudes, the fraction of stars rapidly declines with a contribution of ∼10 per cent for magnitudes $m_{F814W} = 22.5$, which quickly declines, as indicated in the inset panel, until it becomes almost negligible for $m_{F814W} > 23.5$. Extending the analysis to the whole sample, we retrieved an average stellar density of ∼7000 stars per deg^2 (∼450 stars per CCD) for $m_{F814W} < 22.5$.

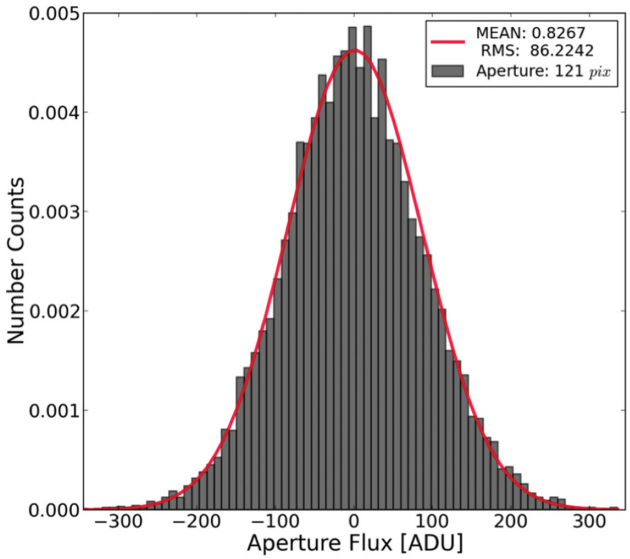

Figure 18. The figures shows an example of the background distribution in 121 pixel apertures after drawing ∼50 000 apertures in blank regions. To estimate the empirical dependence between photometric apertures and the RMS properly, the procedure was repeated spanning a range of apertures between up to 250 pixels, covering the size distribution measured for ALHAMBRA objects.

underestimation of the real photometric uncertainties, critically affecting the photometric depth estimations (the survey photometric limiting magnitude) and the photometric redshift accuracy. We have therefore carefully estimated photometric errors using an empirical approach (similar to that described in Casertano et al. 2000, Labbé et al. 2003, Benítez et al. 2004, Gawiser et al. 2006 and Quadri et al. 2007).

As explained in Section 3.2, ColorPro was updated to degrade automatically every image that has a PSF narrower than that of the detection image. We also rescaled the original NIR images (from OMEGA-2000) to the LAICA pixel size (Cristóbal-Hornillos et al., in preparation). Both procedures alter the properties of their original background distributions. Moreover, when deriving photometric uncertainties, SExtractor always assumes that the image background follows a Poisson distribution with no correlation among pixels. This underestimates the real noise, as we will see below.

To derive empirical photometric uncertainties for each individual image, we mask out the objects detected by SExtractor using the segmentation map derived from the *F*814*W* detection image. Then we throw ∼50.000 apertures over the remaining area, measuring both the enclosed signal and the RMS inside it. The procedure is repeated for apertures in the 1–250 pixel range, correcting appropriately by the total exposure time of the pixels belonging to the aperture using the weight maps. Fig. 18 shows an example of the typical measured background distribution for one pixel. The red line corresponds to the best Gaussian fit to the data.

As expected, the ALHAMBRA images are accurately described by a Poisson distribution on small scales. However as apertures become larger, a second term starts to dominate the distribution, indicating the presence of large-scale correlations among pixels. In this case, the background distribution is described by the relation

$$\sigma(A) = \frac{\sigma_1 \sqrt{N}(C_1 + C_2\sqrt{N})}{\sqrt{w_N}}, \quad (10)$$

where coefficient C_1 indicates the Poisson contribution dominating on small scales, C_2 the contribution on large scales, w_N the corresponding per cent weight (from WEIGHT map) and σ_1 the background distribution measured for one-pixel apertures.

The relevance of this sort of correction can be appreciated in Fig. 19, where the differences between a Poisson-based treatment (solid red line) and an empirically estimated one (solid black line) are shown. Whereas the left panel indicates the dependence of the expected RMS as a function of aperture size $\sqrt{N}$, the right panel shows the re-estimated mean photometric uncertainties as a function of magnitude.

3.8 Photometric verification

As already mentioned in Section 2, we take advantage of the presence in LAICA of four CCDs which simultaneously image close regions of the sky under the same atmospheric conditions and with the same passband to carry out a statistical comparison among contiguous CCDs.

We looked at the number of detected sources per magnitude range and, as illustrated in Fig. 20, the results for the four CCDs were highly consistent for magnitudes $m_{F814W} < 24$, where ALHAMBRA is photometrically complete. For fainter magnitudes, CCD3 showed a decrease in the number of detections, probably due to its poorer efficiency. We also compared the photometric uncertainties between CCDs and again CCD1, CCD2 and CCD4 showed good agreement, whereas CCD3 differed from the general trend, showing larger photometric uncertainties.

Finally, we did not observe any horizontal shifts between curves, indicating no photometric bias at first order. This is illustrated in the right panel of Fig. 20.

4 PHOTOMETRIC REDSHIFTS

The Bayesian Photometric Redshift (BPZ) code implements the Bayesian method of Benítez (2000) to estimate photo-z. BPZ weights the redshift/type likelihood $L(C|z, T)$, obtained from comparison of the redshifted template library with the observed galaxy magnitudes by a prior probability $p(z, T|I)$. $L(C|z, T)$ is often multimodal, due to colour/redshift degeneracies, and the inclusion of prior information helps to eliminate unrealistic solutions and make $p(z, T)$ more compact, improving the photo-z accuracy and reducing the number of catastrophic outliers. In this work, we used an updated version of the code (BPZ2.0, Benítez 2014), which includes several changes with respect to its original version.

BPZ2.0 uses a new library composed of six SED templates originally drawn from Projet d'Étude des GAlaxies par Synthèse Évolutive (PEGASE: Fioc & Rocca-Volmerange 1997) but then recalibrated using FIREWORKS photometry and spectroscopic redshifts (Wuyts et al. 2008) to optimize its performance. In addition to these basic six templates, four GRAphite and SILicate (GRASIL) and one STARBURST template have been added. As seen in the left panel of Fig. 21, this new library includes five templates for elliptical galaxies, two for spiral galaxies and four for starburst galaxies, along with emission lines and dust extinction. The opacity of the intergalactic medium was applied as described in Madau (1995). An example of a typical spectral fitting using the ALHAMBRA photometry is shown in the right panel of Fig. 21. The inset panel corresponds to the resulting redshift distribution function $p(z)$. The library and the procedure to obtain it will be described in detail in Benítez (2014).

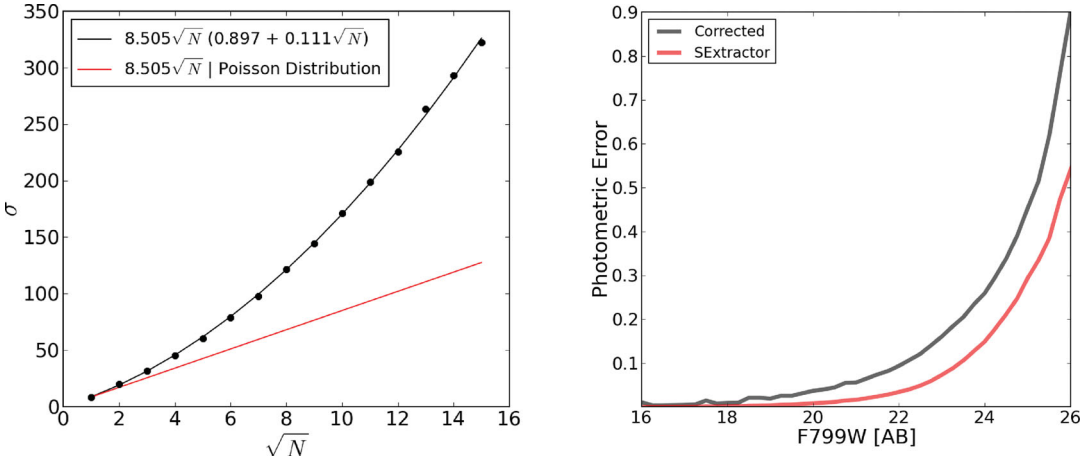

Figure 19. Photometric uncertainties. The figure shows the differences between the photometric uncertainties yielded by SEXTRACTOR (solid red line), assuming that the background follows a Poisson distribution and those empirically estimated (solid black line) using the methodology described in Section 3.7. The left panel illustrates how the dependence between the RMS and the aperture size ($\sqrt{N}$) becomes progressively underestimated by SEXTRACTOR, due to the presence of large-scale correlations among pixels introduced during image processing. As described in equation 10, the number outside the parentheses in the legend corresponds to the background RMS derived for one-pixel apertures and the number inside corresponds to that for the (Poisson) contribution; these dominate on small and large scales respectively. The right panel compares the average photometric uncertainties as a function of magnitude, both derived by SEXTRACTOR (solid red line) and using the empirical approach described in the text (solid black line). As expected, SEXTRACTOR underestimates the real photometric errors, which become especially significant at faint magnitudes.

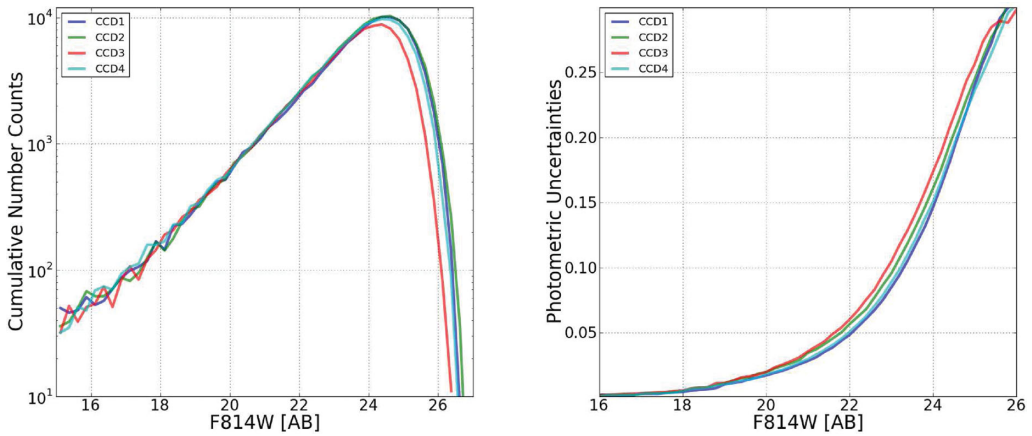

Figure 20. Internal photometric verifications. Using the advantage that the four CCDs composing the LAICA optical system were simultaneously imaging (almost) the same regions of the sky, under equal atmospheric conditions and through the same passband, we performed internal photometric comparisons among the CCDs. As seen in the left panel, on the one hand we compared number counts per magnitude range to ascertain the homogeneity during the detection process. As expected, whereas CCD1, CCD2 and CCD4 were similar, CCD3 behaved slightly worse, with a shallower photometric depth. The lack of either bumps or horizontal shifts among CCDs indicated homogeneous detections and no photometric zero-point offsets. On the other hand, we also compared the photometric uncertainties as a function of the magnitude for the four CCDs, as seen in the right panel. As expected, CCD3 typically showed larger photometric uncertainties, confirming its poorer performance.

Likewise, the BPZ2.0 also includes a new prior, which gives the probability of a galaxy with apparent magnitude m_0 having a certain redshift z and spectral type T. The prior has been empirically derived for each spectral type and magnitude by the redshift distributions measured in the GOODS–MUltiwavelength Southern Infrared Catalog (MUSIC: Santini et al. 2009), COSMOS (Scoville et al. 2007) and Ultra-Deep Field (UDF: Coe et al. 2006) catalogues.

In addition, the BPZ2.0 also provides an estimation of the galaxy stellar mass, calculated from the assigned interpolated spectrum of the galaxy by applying the colour–M/L ratio relationship established by Taylor et al. (2011) to the BPZ templates. For an in-depth discussion, we refer the reader to Benítez (in preparation). We performed two different checks to show the robustness of the BPZ stellar masses. First, when comparing the BPZ stellar masses with the masses measured by Bundy et al. (2006) for the COSMOS field, we observed that the uncertainties are within those expected from their analysis (about 0.1–0.2 dex) with a moderate dependence on spectral type, as seen in Fig. 22. Secondly, we obtained BPZ stellar masses from a semi-analytical simulation (Merson et al. 2013; Ascaso et al., in preparation) and compared them with the input masses after correcting them for the effect of different initial mass functions (IMFs; Bernardi et al. 2010). The mean value of the difference is

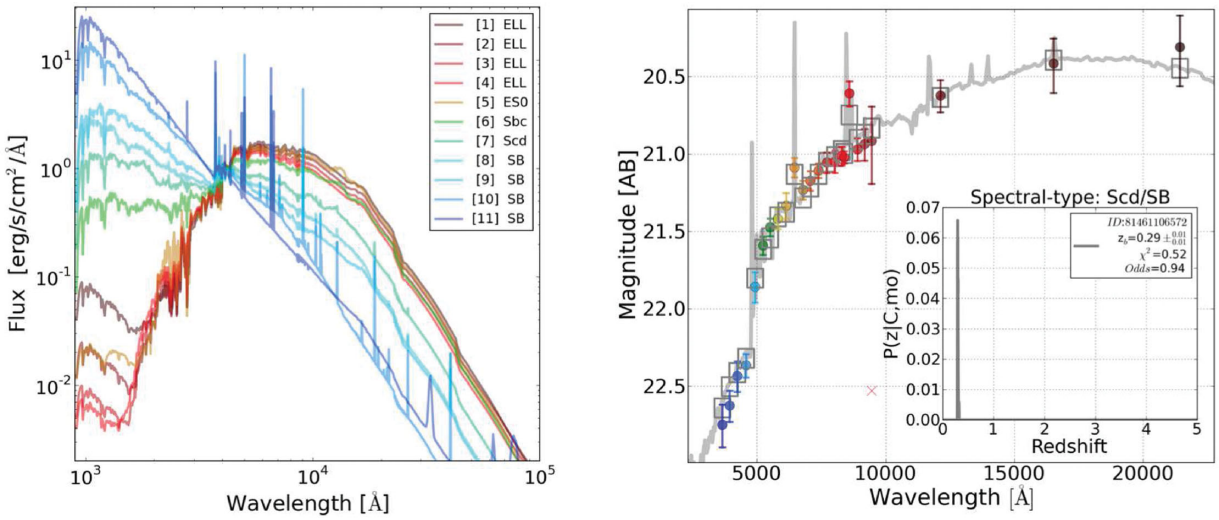

Figure 21. We relied on an updated version of the BPZ code (BPZ2.0) to derive the photometric redshifts. Left: BPZ2.0 includes a new library composed of 11 galaxy templates – five originally drawn from PEGASE, five from GRASIL and one STARBURST. To make its visualization easier, the SEDs were arbitrarily normalized to 4000 Å. The numerical notation used in the catalogues for the BPZ templates is indicated in the legend. Right: this panel shows an example of a typical spectral fitting using the ALHAMBRA photometry, where the inset panel corresponds to its resulting redshift distribution function $p(z)$.

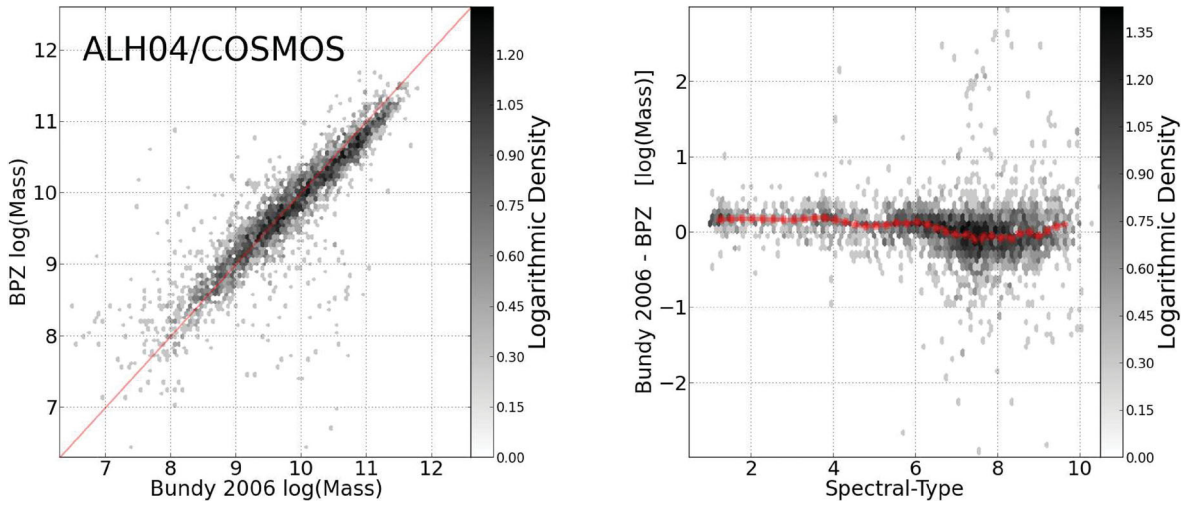

Figure 22. The new version of BPZ provides an estimation of the galaxy stellar mass, calculated from the assigned interpolated spectrum, by applying the colour–M/L ratio relationship established by Taylor et al. (2011) to the BPZ templates. Left: we show a comparison between the BPZ stellar masses with the masses measured by Bundy et al. (2006) for a sample of galaxies from the COSMOS field. We observe that the uncertainties (of about 0.1–0.2 dex) are within those expected by Bundy et al. (2006). Right: we represent the former comparison as a function of spectral type. Again, a moderate dependence is observed, with uncertainties within 0.1–0.2 dex.

$\sim 0.13 \pm 0.30$ dex which, as before, is consistent with the uncertainties reported (Mitchell et al. 2013), confirming the reliability of the stellar mass estimations.

BPZ2.0 provides an estimate for the galaxy redshift, generally defined as $z_b = \sum_T \int dz\, z\, p(z, T)$, and also the spectral type at that redshift, $T_b = [\sum_T p(T|z_b)\, T]/[\sum_T p(T|z_b)]$. To characterize the quality of the photo-z, BPZ provides the *Odds* parameter (Benítez 2000), $Odds = \sum_T \int_{-0.0125(1+z_b)}^{0.0125(1+z_b)} p(z - z_b, T)$. It is worth emphasizing that *Odds* makes it possible to derive high-quality samples with very accurate redshifts and a very low rate of catastrophic outliers. We used a redshift resolution $DZ = 0.001$ for the $0.001 < z < 7.0$ range. In order to cover the spectral-type space fully, we used an interpolation factor between templates of 7, i.e. generated seven models by linear interpolation in the flux space in between each of the original 11 models. The redshift confidence interval provided by *zb_min* and *zb_max* corresponds to 68 per cent of the probability distribution function. Note that, for multimodal probabilities, $p(z)$ can tend to 0 within this range.

4.1 Photometric redshift accuracy

The normalized median absolute deviation (NMAD) is a robust measurement of the accuracy reached by a sample of photometric redshifts (Brammer, van Dokkum & Coppi 2008). A typical photometric redshift error distribution has fat tails, clearly departing from a pure Gaussian distribution, in addition to a relatively large fraction of outliers. The NMAD estimator manages to get a stable estimate of the spread of the core of photo-z distribution without

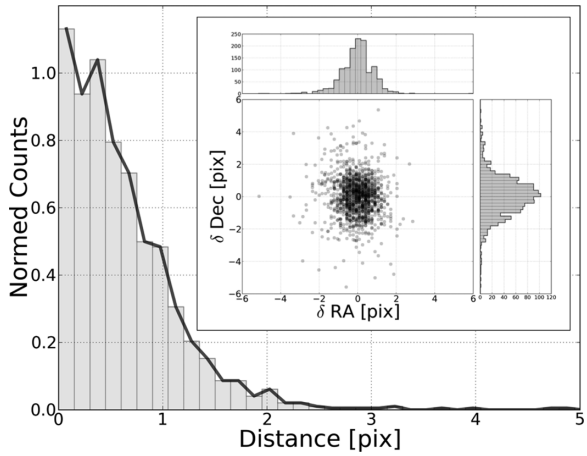

Figure 23. Astrometric matching with spectroscopic samples. In order to reduce the fraction of potential mismatched galaxies, we initially performed second-order astrometric corrections between the ALHAMBRA fields and other surveys, to establish a maximum distance of ∼3 pixel (<0.7 arcsec) to match our detections. This maximum separation was set manually for each survey, being the distance at which the radial matching distribution reached its first minimum. As seen in the main panel, ∼60 per cent of the selected spectroscopic sample is well accommodated within a one-pixel distance. The inset panel illustrates the astrometric dispersion between ALHAMBRA and the overlapping surveys in terms of δRA ($\mathrm{RA^{ALH}} - \mathrm{RA^{surv}}$) and δDec ($\mathrm{Dec^{ALH}} - \mathrm{Dec^{surv}}$) in units of pixels.

being affected by catastrophic errors. The NMAD is defined as follows:

$$\sigma_{\mathrm{NMAD}} = 1.48 \times \mathrm{median}\left(\frac{|\delta z - \mathrm{median}(\delta z)|}{1+z_{\mathrm{s}}}\right) \quad (11)$$

and

$$\delta z = z_{\mathrm{b}} - z_{\mathrm{s}}, \quad (12)$$

where z_{b} corresponds to the Bayesian photometric redshift and z_{s} to the spectroscopic redshift. Along with the scatter, it is also important to quantify both the presence of any systematic bias μ and the fraction of catastrophic errors. In this work, we use two different definitions for the outlier rate:

$$\eta_1 = \frac{|\delta z|}{1+z_{\mathrm{s}}} > 0.2, \quad (13)$$

$$\eta_2 = \frac{|\delta z|}{1+z_{\mathrm{s}}} > 5 \times \sigma_{\mathrm{NMAD}}. \quad (14)$$

As explained in Section 2, ALHAMBRA was designed to partially overlap with fields observed by other surveys with extensive spectroscopic coverage. We compiled a sample of ∼7200 galaxies with spectroscopic redshifts from the publicly available data by selecting high-quality (secure) objects with a good astrometric match to our data. The first condition is essential to estimate our outlier rate accurately, even if it slightly biases our sample towards the brightest magnitudes, since, as Fernández-Soto et al. (2001) established, low-quality spectroscopy can be much more unreliable than photo-z. To implement the second condition, we derived accurate astrometric corrections between samples (to avoid any offset) and then established a maximum matching distance of ∼3 pixel (<0.7 arcsec), as shown in Fig. 23. This maximum separation was manually set for each survey, being the distance at which the distribution of matching distances reached its first minimum. As seen in Fig. 24, the compiled redshift sample shows a mean redshift $\langle z_{\mathrm{s}} \rangle \sim 0.77$ and a mean magnitude (based on ALHAMBRA photometry) $m_{F814W} \sim 22.3$. In Table 4, the contribution from each survey is specified, indicating the number of selected galaxies, mean magnitude and redshift.

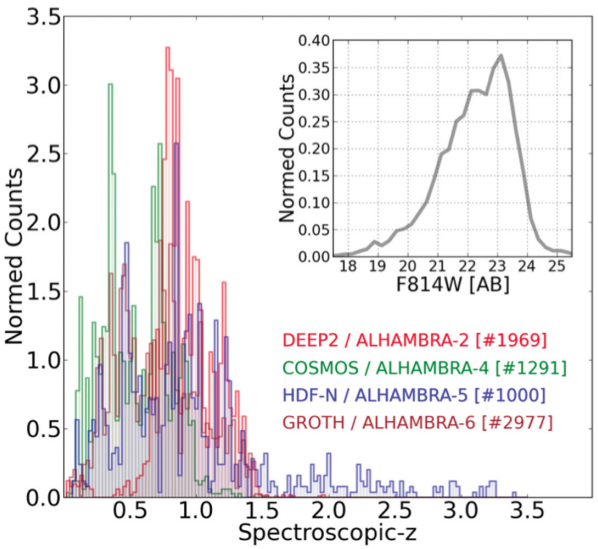

Figure 24. Spectroscopic redshift compilation. Given the overlap between the ALHAMBRA fields and other existing spectroscopic surveys, we compiled a sample of ∼7200 galaxies with secure spectroscopic redshifts to quantify the accuracy for our photometric redshifts. Each survey contribution is colour-coded (for visualization), as indicated in the legend. As seen in the figure, the compiled redshift sample mostly covers the ALHAMBRA parameter space, showing a redshift range $0 < z_{\mathrm{s}} < 1.5$ (with a mean redshift $\langle z_{\mathrm{s}} \rangle \sim 0.77$) and a magnitude range (based on ALHAMBRA photometry) $18 < m_{F814W} < 25$ (with a mean magnitude $m_{F814W} \sim 22.3$).

Table 4. Spectroscopic redshift samples.

#	Survey	Reference	$\langle m_{F814W} \rangle$	$\langle z \rangle$
1269	DEEP-2	Koo et al. (1995)	22.64	0.92
1291	COSMOS	Lilly et al. (2009)	21.36	0.54
1000	GOODS-N	Cooper et al. (2011)	22.75	0.83
2977	GROTH	Davis et al. (2007)	22.21	0.70
7237			22.24	0.75

As seen in Fig. 25, when compared with the spectroscopic sample, our photometric redshift estimations show a dispersion $\sigma_z = 0.0106$ for $m_{F814W} < 22.5$ with a fraction of catastrophic outliers $\eta_1 \sim 2.7$ per cent. For fainter magnitudes $m_{F814W} < 24.5$, the accuracy observed is $\sigma_z = 0.0134$ and the fraction of catastrophic outliers $\eta_1 \sim 4.0$ per cent. The fraction of catastrophic outliers dramatically decreases when selecting a more restricted sample (excluding X-ray emitters, active galactic nuclei (AGNs) or detections observed in only a few bands). In addition, the photo-z error and the fraction of catastrophic outliers decrease rapidly as the *Odds* interval increases. We show the expected accuracy for the photometric redshifts as a function of redshift, $F814W$ magnitude and *Odds* range in Fig. 26. A more detailed analysis can be found in Tables 5, 6 and 7, respectively.

In order to verify that $\delta_z/(1+z_{\mathrm{s}})$ is representative for the spectroscopic sample, the cumulative distribution of sources is represented in Fig. 27. We observed that ∼64 and ∼90 per cent of the photometric redshifts are well fitted within the formal 1σ and 2σ confidence

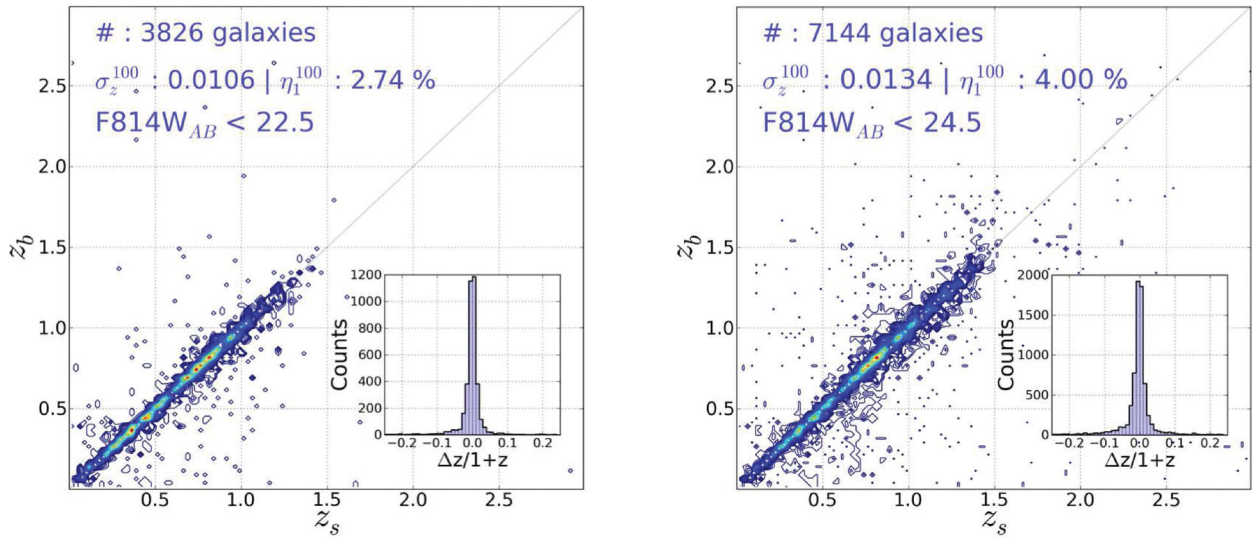

Figure 25. Photometric redshift accuracy. The figures show the comparison between the ALHAMBRA photometric redshift z_b and the spectroscopic redshift z_s, along with the error distribution $\Delta_z/(1+z)$, for two different magnitude ranges. The left plot shows the accuracy obtained for the bright sample ($m_{F814W} < 22.5$) with $\sigma_z < 0.0106$ and a fraction of catastrophic outliers $\eta_1 \sim 2.7$ per cent, while the right plot shows $\sigma_z < 0.0134$ and a fraction of catastrophic outliers $\eta_1 \sim 4.0$ per cent when including the entire sample. In both cases, the fraction of catastrophic outliers (defined in Section 4.1) decreases dramatically when selecting galaxies with higher *Odds*, as indicated in Table 7.

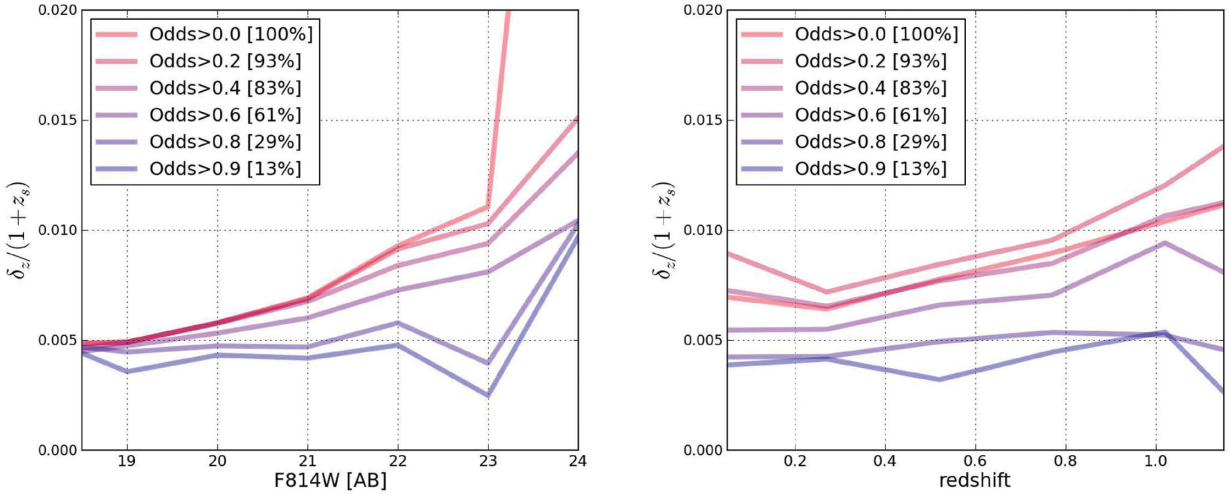

Figure 26. Photometric redshift accuracy as a function of apparent magnitude *F*814*W* (left panel) and spectroscopic redshift (right panel). We explored the expected accuracy for our photometric redshifts in terms of a specific magnitude range and redshift range, applying different *Odds* intervals.

intervals, respectively. This indicates that the uncertainties in z_b are quite realistic.

Applying the same approach explained in Section 3.8, we performed internal photometric redshifts checks to compare our results between contiguous CCDs. As illustrated in Fig. 28, the statistical results were consistent between CCDs, showing a scatter within the intrinsic variance for the sample observed by each CCD.

4.2 Photometric zero-point recalibration

4.2.1 Photometric ZP calibrations using spectroscopic redshifts

As was shown in Coe et al. (2006), by comparing the observed colours of galaxies with spectroscopic redshifts against those expected from an empirically defined photo-z library, it is possible to calibrate photometric zero-points to within a few per cent, an accuracy similar to or better than that reached by standard, stellar-based calibration techniques. This capability has been included in the BPZ software package from its initial release (Benítez 2000) and has been applied successfully to several data sets (Capak et al. 2007; Hildebrandt, Wolf & Benítez 2008).

To calibrate the ALHAMBRA zero-points, we followed this procedure for each individual CCD. First, we selected the spectroscopic redshift galaxies detected in all 24 bands with $S/N > 10$, and chose the BPZ template that best fits its colours at their redshift. We then calculated the ratios between the fluxes predicted in each band by the templates and those observed; the median ratio, converted to a magnitude, represents the zero-point offset (ZPO) required to match the observed magnitudes to the expected ones. We then corrected the fluxes by this value and iterated until the process converged and

Table 5. Photometric redshift quality versus spectroscopic redshifts.

Spectroscopic Redshift	σ_z (Odds > 0.0)	# (per cent)	η_1 (per cent)	η_2 (per cent)	σ_z (Odds > 0.5)	# (per cent)	η_1 (per cent)	η_2 (per cent)	σ_z (Odds > 0.9)	# (per cent)	η_1 (per cent)	η_2 (per cent)
$0.00 < z < 0.25$	0.0115	10.8	0.4	0.8	0.0086	3.8	0.1	0.2	0.0056	0.3	0.0	0.0
$0.25 < z < 0.50$	0.0101	21.0	0.6	1.5	0.0087	10.5	0.2	0.4	0.0062	1.6	0.0	0.1
$0.50 < z < 0.75$	0.0136	19.6	1.0	2.4	0.0107	11.5	0.3	0.8	0.0061	1.2	0.1	0.1
$0.75 < z < 1.00$	0.0135	21.4	0.7	2.3	0.0104	12.7	0.2	0.7	0.0066	1.4	0.0	0.1
$1.00 < z < 1.25$	0.0171	13.2	0.4	1.3	0.0125	7.0	0.1	0.4	0.0070	0.3	0.0	0.0
$1.25 < z < 1.50$	0.0194	7.2	0.3	0.9	0.0132	2.3	0.1	0.3	–	–	–	–
$1.50 < z < 1.75$	0.0988	3.4	0.1	0.2	0.0567	0.3	0.0	0.0	–	–	–	–
$1.75 < z < 2.00$	0.1078	1.4	0.2	0.4	0.1620	0.0	0.0	0.1	–	–	–	–

Table 6. Photometric redshift quality versus *F*814*W* magnitude.

Magnitude F814W	σ_z (Odds > 0.0)	# (per cent)	η_1 (per cent)	η_2 (per cent)	σ_z (Odds > 0.5)	# (per cent)	η_1 (per cent)	η_2 (per cent)	σ_z (Odds > 0.9)	# (per cent)	η_1 (per cent)	η_2 (per cent)
$18.0 < m < 19.0$	0.0081	0.8	0.0	0.1	0.0073	0.6	0.0	0.0	0.0055	0.1	0.0	0.0
$19.0 < m < 20.0$	0.0083	2.2	0.1	0.3	0.0077	1.7	0.1	0.1	0.0056	0.3	0.1	0.1
$20.0 < m < 21.0$	0.0095	5.3	0.3	0.7	0.0085	4.1	0.1	0.3	0.0059	0.7	0.0	0.0
$21.0 < m < 22.0$	0.0101	11.9	0.4	1.1	0.0093	9.0	0.2	0.5	0.0058	1.3	0.0	0.0
$22.0 < m < 23.0$	0.0140	26.0	0.7	2.1	0.0111	16.0	0.3	0.9	0.0065	1.5	0.0	0.0
$23.0 < m < 23.5$	0.0182	22.8	0.6	2.1	0.0129	9.4	0.2	0.6	0.0045	0.5	0.0	0.0
$23.5 < m < 24.0$	0.0263	30.7	0.9	2.3	0.0118	7.4	0.2	0.4	0.0038	0.3	0.0	0.0

Table 7. Photometric redshift accuracy versus Odds for the global sample.

Interval	Sample[a] (per cent)	σ_z	η_1 (per cent)	η_2 (per cent)
Odds > 0.00	1.00	0.0137	3.04	8.64
Odds > 0.10	0.91	0.0131	2.56	7.36
Odds > 0.20	0.80	0.0123	2.13	6.01
Odds > 0.30	0.71	0.0116	1.71	5.00
Odds > 0.40	0.61	0.0109	1.46	4.09
Odds > 0.50	0.50	0.0102	1.08	2.89
Odds > 0.60	0.36	0.0093	0.72	1.86
Odds > 0.70	0.24	0.0082	0.51	1.13
Odds > 0.80	0.14	0.0069	0.30	0.57
Odds > 0.90	0.07	0.0062	0.15	0.23
Odds > 0.95	0.03	0.0057	0.08	0.14

[a] $m_{F814W} < 24$.

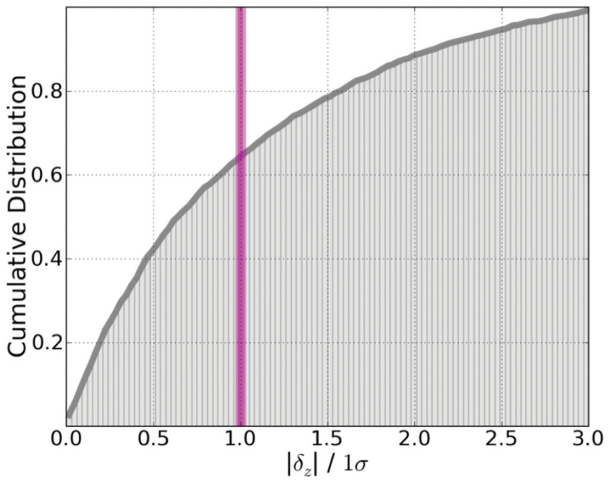

Figure 27. Cumulative distribution of the ratio $|\delta z|/1\sigma$. We observed that ∼64 and ∼90 per cent of the photometric redshifts are well fitted within the formal 1σ (magenta vertical line) and 2σ confidence intervals, respectively. This indicates that the photometric redshift uncertainties have been reliably established.

the calculated correction was below 1 per cent in all filters. Since all these changes are relative by nature, the synthetic *F*814*W* images were taken as anchor of the whole system.

Another useful quantity calculated by BPZ is the excess photometric scatter over the expected photometric error, what we call zero-point error (ZPE). This noise excess could be due to two sources: a systematic mismatch between the templates and real galaxy colours or a systematic error in the photometry. As Benítez (2014) shows, if enough spectroscopic redshifts are present, averaging over many templates and different SED rest-frame locations ensures that such residuals are typically due to flaws in the photometry. Including this factor allows for a much more realistic estimate of the error and significantly improves the photo-z precision.

We explored the dependence of the amplitude of these zero-point corrections on several observational variables. Looking for possible systematic effects in the reduction, in Fig. 29 we plot globally the zero-point corrections for the ∼1100 individual images as a function of the airmass (top left panel), stellar symmetry (top right panel; defined as the ratio of a/b parameters (Table C1), FWHM scatter (bottom left panel) and the differences between PSF models and stars (top left panel). The procedure was repeated using three different photometric apertures (SEXTRACTOR_*ISOphotal* as red circles, SEXTRACTOR_*AUTO* as blue circles and SEXTRACTOR_*APER* (3 arcsec) as magenta circles) to discard any dependence on the sampled area. As indicated by the mean value of the distributions (dashed black lines), we did not observe any clear correlations, with typical fluctuations smaller than 1 per cent.

We explored whether zero-point offsets depended on the magnitude. For that, we split the spectroscopic sample into two equal-sized groups with galaxies brighter and fainter than $m_{F814W} = 22.5$. As seen in Fig. 30 (blue dots) the corrections derived for both samples are the same, within the typical level of photometric uncertainties. Even though filter *F*954*W* showed a clear disagreement among

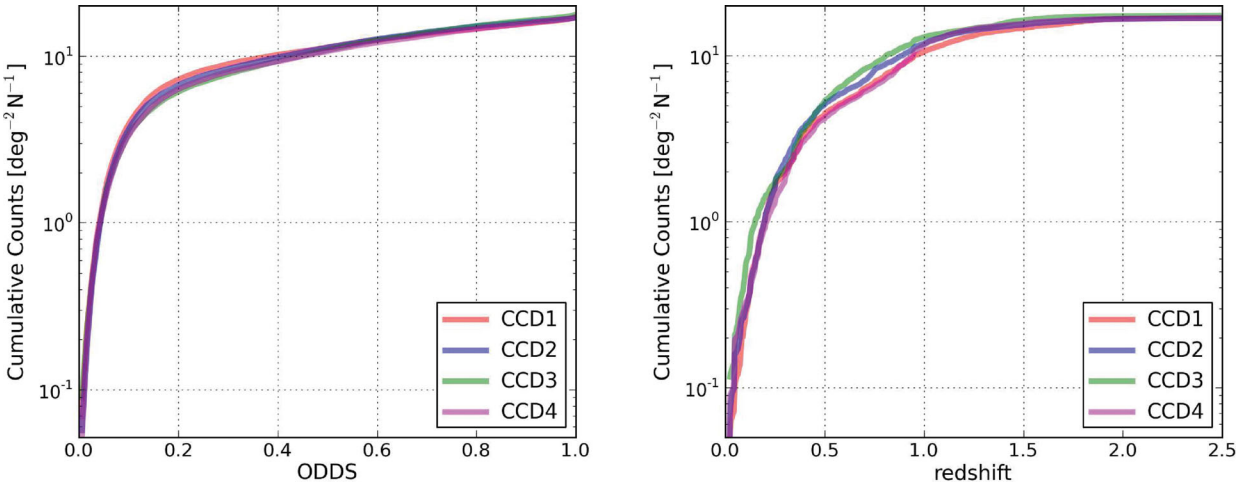

Figure 28. Internal photometric redshift checks. Following the same approach as explained in Section 3.8, we systematically compared the *Odds* (left panel) and photometric redshift z_b (right panel) distributions among contiguous CCDs. The statistical results were consistent between each other, with a scatter within the expected intrinsic variance for the sample imaged by each detector. These tests served to ascertain the homogeneity within the different fields.

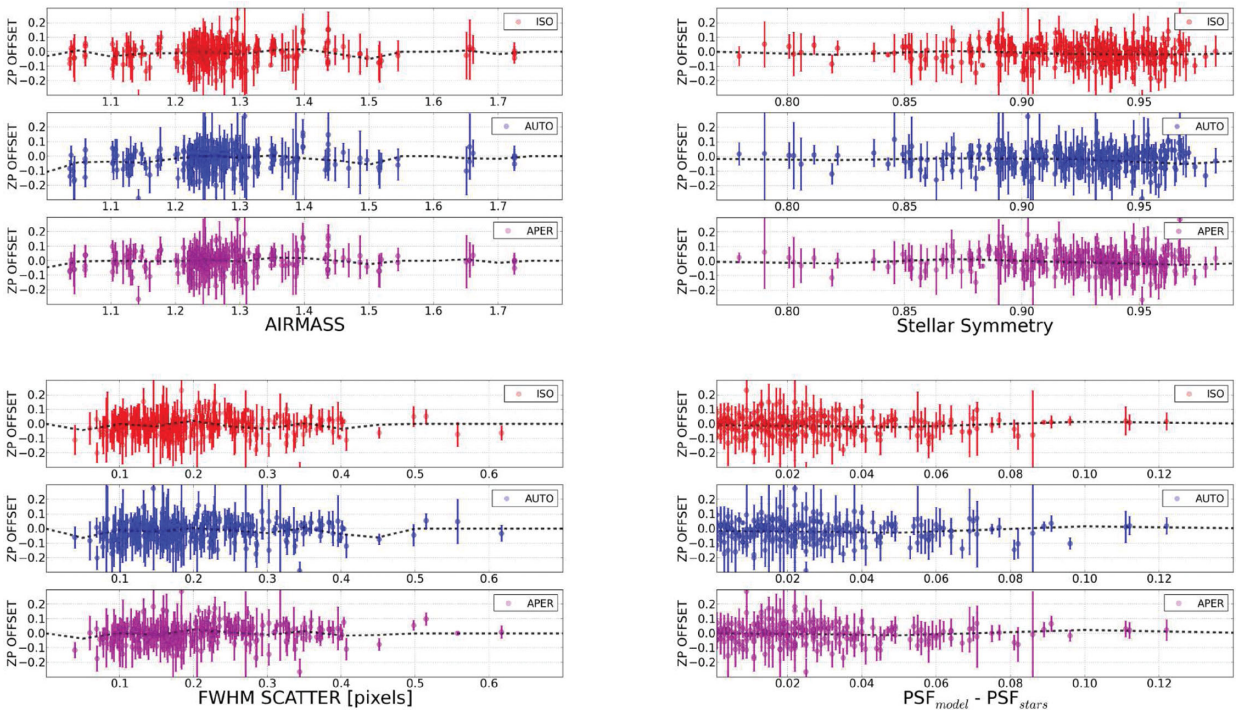

Figure 29. Photometric zero-point validations. We studied the source of the photometric zero-point corrections (derived using SED-fitting algorithms) by comparing these quantities with several observational variables. Considering the possibility of a systematic effect during the data reduction, we represented the corrections for the ∼1100 individual images globally as a function of AIRMASS (top left panel), Stellar Symmetry (top right panel), FWHM scatter (bottom left panel) and the differences between PSF models and stars (top left panel). The procedure was repeated using three different photometric apertures (SEXTRACTOR_*ISOphotal* as red circles, SEXTRACTOR_*AUTO* as blue circles and SEXTRACTOR_*APER* (3 arcsec) as magenta circles) to discard any systematic effect due to the galaxy sampling regions. As indicated by the mean value of the distributions (dashed black lines), no clear correlations were observed, with fluctuations smaller than 1 per cent.

samples, its scatter was as large as ∼0.3 mag, indicating other sort of problems, perhaps related to the reductions. To look for a dependence on the photometric aperture size due to some effect related to the PSF corrections, we again divided the spectroscopic sample into two equal-sized groups with photometric areas smaller (and larger, respectively) than 125 pixels. As seen in Fig. 30 (green dots), differences among samples were smaller than 1 per cent.

Finally, the dependence between redshift range and zero-point offsets was also considered, assuming a possible effect due to evolution in the galaxy populations (since the BPZ templates do not include any evolution). As seen in Fig. 30 (magenta dots), the differences obtained from both samples were smaller than 1 per cent and so within the error-bar regime. We therefore conclude that the zero-point offsets do not depend on the photometric treatment and

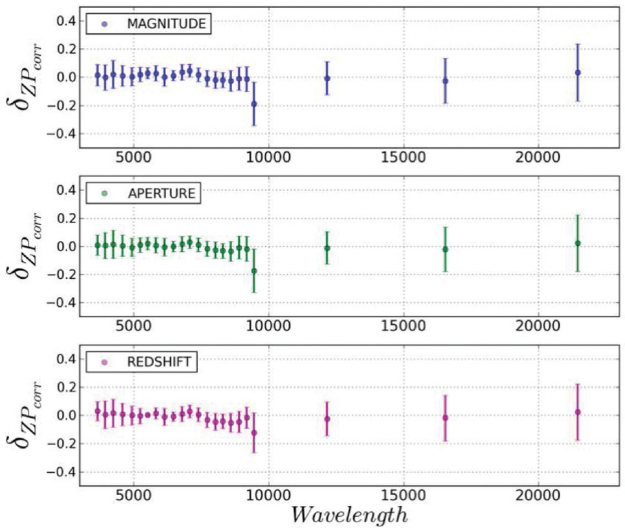

Figure 30. Photometric zero-point validations II. We also studied the robustness of the photometric zero-point corrections using different samples of galaxies. We split the spectroscopic sample into equal-sized groups based on its magnitude ($m_{F814W} < 22.5$ and $m_{F814W} > 22.5$), aperture size (area <125 pixels and area >125 pixels) and redshift ($z < 0.81$ and $z > 0.81$) and derive new photometric zero-point corrections using BPZ. As observed in the figure, for all three cases, the differences among samples (δ_{ZP}) are quite small. This result shows that the zero-point corrections we derive do not depend strongly on the redshift range or spectral type and therefore are indicative of true offsets in the zero-points, most likely due to the differences between the calibrations obtained from traditional colour transformations based on stars and the average colours of galaxies as defined by the BPZ template set, calibrated with *Hubble Space Telescope* (*HST*) observations.

represent real offsets between the zero-points defined by the colours of the BPZ templates calibrated with the FIREWORKS *HST* photometry and those defined by the stellar-based colour calibrations used for the primary ALHAMBRA photometric calibration.

4.2.2 Photometric zero-point calibrations using photometric redshifts

Although ALHAMBRA was designed to overlap with other spectroscopic surveys, only ∼40 per cent of its fields had enough galaxies with spectroscopic redshifts to derive zero-point corrections, as described above. As discussed in Section 4.2.1, the absence of any clear dependence on the observational parameters made infeasible any extrapolations between different fields. Given the obvious improvement resulting from the zero-point corrections, this lack of calibration spectroscopy created a serious source of inhomogeneity across the survey.

We realized that the photometric redshifts obtained for emission-line galaxies were quite robust to changes in the zero-point calibration and therefore, statistically, we could treat those redshifts as spectroscopic for calibration purposes, obtaining an automatic source of zero-point corrections for all our fields. Thus, we ran BPZ on the photometric catalogues with the original, stellar-based zero-point estimations. Then we selected a sample formed by those galaxies observed in all 24 filters, with large S/N ($m_{F814W} < 23.0$), good fit to the SED ($Odds \geq 0.9$ and $\chi^2 \leq 1$) and classified by BPZ.2 as late-type galaxies ($T_b > 7$). We apply the procedure described in Section 4.2.1, using the photometric redshifts as spectroscopic values and iterating until convergence is reached. This is basically equivalent to calibrating the ZP using the continuum of ELGs as defined by the BPZ.2 templates.

In the top panel of Fig. 31, we show the photometric redshift accuracy obtained with three different calibration methods: the original zero-points (red line), corrections derived from photometric redshifts (blue line) and corrections from spectroscopic redshifts (green line). The results indicate that the methodology presented here improves the photometric redshift accuracy successfully almost up to the level provided by the spectroscopic sample and also dramatically reduces the fraction of catastrophic outliers. The bottom panel of Fig. 31 shows how the corrections derived with late-type galaxies worked very well for early-type galaxies, proving that they are independent of the particular choice of templates in the library. It is worth noting that even if the accuracy reached by this method was always slightly worse than that provided by a real spectroscopic sample, it was always much better than the standard stellar-based calibration. Therefore, we decided to apply this kind of zero-point calibration for all fields without spectroscopy, which significantly improved the overall homogeneity of the ALHAMBRA sample. This kind of calibration promises to have wide application to future narrow-band surveys such as Javalambre Physics of the Accelerating Universe (JPAS: Benítez et al. 2009; Benítez et al. 2014).

4.3 Photometric redshift distributions

Despite having a relatively small field of view (FOV) compared with other, much larger surveys, one of the main virtues of ALHAMBRA is that it includes eight different lines of sight widely separated, which provides a realistic estimation of both the typical redshift distribution of galaxies across cosmic time and its inherent variability (cosmic variance).

Photometric redshifts are probabilistic by nature and the shape of the probability distribution is usually far from a well-behaved Gaussian. Therefore point estimates of the redshift and other parameters have limited value and it is much safer to work with the full probability distribution $p(z, T|C)$ (Benítez 2000; Coe et al. 2006; Mandelbaum et al. 2008; Cunha et al. 2009; Wittman 2009; Bordoloi, Lilly & Amara 2010; Abrahamse et al. 2011; Sheldon et al. 2012). This is specially true for most faint galaxies, with noisy photometric information, where probability distributions usually become multimodal and completely asymmetric. Even in those cases, the distribution $p(z, T|C)$ obtained with a properly calibrated library and prior can be relied upon to produce accurate population properties like the redshift distribution.

We therefore define the global photometric redshift distribution $P(z)$ as follows:

$$P(z) = \sum_{i=1}^{N_g} P_i(z) = \sum_{i=1}^{N_g} \left[\int \mathrm{d}z \sum_T p_i(z, T|C) \right], \quad (15)$$

where $p_i(z, T)$ represents the redshift/type probability distribution function for the ith galaxy.

We also ran BPZ on the photometric catalogue used by Ilbert et al. (2009) to derive the global redshift probability distribution function $P(z)$ for the COSMOS field and compare it consistently with our results. We first looked at the $P(z)$ derived using the ALHAMBRA-4/COSMOS data (red line) with the $P(z)$ derived using the COSMOS data (blue line), as seen in the left panel of Fig. 32, where both distributions consistently reproduce a double peak at redshifts $z \sim 0.3$ and $z \sim 0.9$, respectively. However,

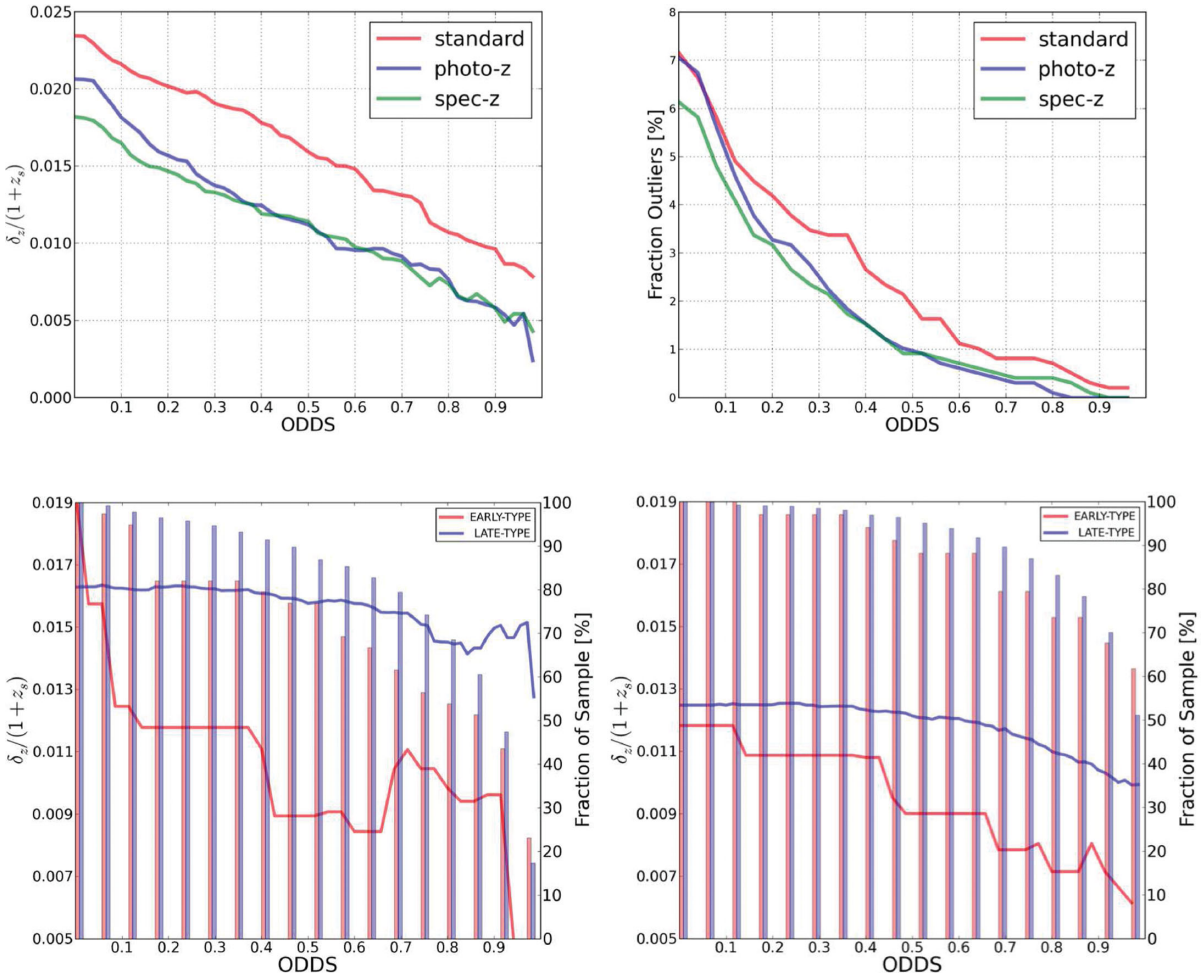

Figure 31. We compare the spectroscopic redshifts with photo-z obtained after applying zero-point corrections with three different approaches: using the standard stellar-based method (red line), photometric redshifts derived from emission-line galaxies (blue line) and a spectroscopic redshift sample (green line). As seen in the top left panel, photometric redshifts using emission-line galaxies not only are a vast improvement with respect to the stellar-based method but also get quite close, in terms of accuracy, to the level of precision achieved by using the highest quality spectroscopic redshifts (*Odds* > 0.3). In addition, the fraction of catastrophic outliers with high *Odds* was also significantly reduced, as shown in the top right panel. In the two bottom panels we compare how the zero-point corrections derived with the emission-line galaxies (late-type) affect both main galaxy types. We show the dependence of both the accuracy (left scale) and the outlier rate (right scale) before (left bottom panel) and after (bottom right panel) applying the zero-point corrections. Not only has the accuracy for the late-type galaxies (solid blue line) improved significantly with the corrections but also that of the early-type galaxies (solid red line). Meanwhile, the fraction of galaxies per *Odds* interval (vertical bars) increased homogeneously among spectral types, indicating that the calibration also produced more galaxies with high quality photo-z.

whereas the ALHAMBRA-4 field shows a mean redshift $\langle z\rangle = 0.60$ for $m_{F814W} < 22.5$ and $\langle z\rangle = 0.87$ for $m_{F814W} < 25.5$, the COSMOS field shows a mean redshift $\langle z\rangle = 0.66$ for $m_{F814W} < 22.5$ and $\langle z\rangle = 0.96$ for $m_{F814W} < 25.5$, as seen in the right panel of Fig. 32. Meanwhile, the global photometric redshift distribution derived for all seven ALHAMBRA fields (excluding stars) shows a mean redshift $\langle z\rangle = 0.56$ for $m_{F814W} < 22.5$ and $\langle z\rangle = 0.85$ for $m_{F814W} < 25.5$, as seen in the right panel of Fig. 33. This result indicates that, as is known, the COSMOS field shows a clear overdensity with respect to the mean value derived by averaging the seven ALHAMBRA fields. In fact, the average galaxy number in COSMOS goes up by 60 per cent between $z = 0.4$ and $z = 0.7$, whereas no such effect is observed in our average.

To study the evolution of the number counts as a function of the magnitude $F814W$ and redshift, we derived the averaged redshift probability distribution function for the ALHAMBRA fields. As seen in the left panel of Fig. 34, the solid red line corresponding to the mean redshift distribution (per bins of 0.5 mag) indicates a clear evolution moving from $\langle z\rangle \sim 0.2$ for $m_{F814W} < 20.5$ to $\langle z\rangle \sim 0.8$ for $m_{F814W} > 23.0$. Inversely, the right panel of Fig. 34 shows how the peak of the averaged distribution of galaxies increases as a function of the redshift for different magnitude ranges.

We explored the variance in the redshift–magnitude distribution of galaxies as a function of the absolute B magnitude and spectral type. As seen in Fig. 35, we split the sample into early-type galaxies (top panel, defined as $1 < T_b < 5$) and late-type galaxies (bottom panel, defined as $7 < T_b < 11$). We plot the redshift distribution for each of the seven individual ALHAMBRA fields (A_i) and one averaged (*Global*) sample. As observed from the figure, where the logarithmic density was colour-coded, individual structures clearly seen in each individual field are smoothed over in the global distribution. In particular, the well-known bimodal distribution in the COSMOS field (A4) is not systematically observed in the other fields.

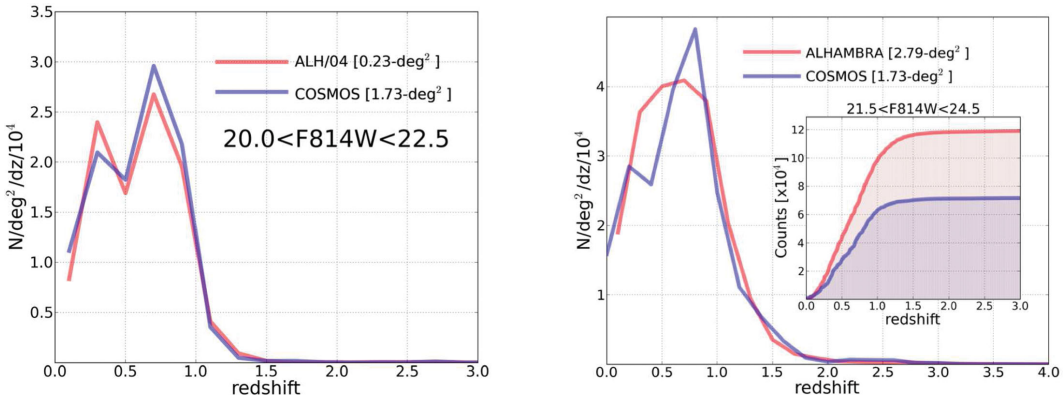

Figure 32. Comparison of the redshift probability distribution function $P(z)$ for ALHAMBRA and the COSMOS field. We run BPZ on the Ilbert et al. (2009) catalogue in the same way we did for our ALHAMBRA fields and generate the corresponding $P(z)$. As seen in the left panel, the $P(z)$ for ALHAMBRA-04/COSMOS (red line) and COSMOS (blue line) are quite similar: both distributions consistently reproduce a double peak at redshifts $z \sim 0.3$ and $z \sim 0.9$. The average redshifts are also similar: ALHAMBRA-4 has $\langle z \rangle = 0.60$ for $m_{F814W} < 22.5$ and $\langle z \rangle = 0.87$ for $m_{F814W} < 25.5$, whereas the COSMOS field shows a mean redshift $\langle z \rangle = 0.66$ for $m_{F814W} < 22.5$ and $\langle z \rangle = 0.96$ for $m_{F814W} < 25.5$. The global $P(z)$ derived averaging the seven ALHAMBRA fields shows a mean redshift $\langle z \rangle = 0.56$ for $m_{F814W} < 22.5$ and $\langle z \rangle = 0.85$ for $m_{F814W} < 25.5$, as seen in the right panel. It is obvious that the COSMOS field has a peculiar distribution, with a peak-through-peak structure that mimics a large evolution effect between $z = 0.4$ and $z = 0.9$.

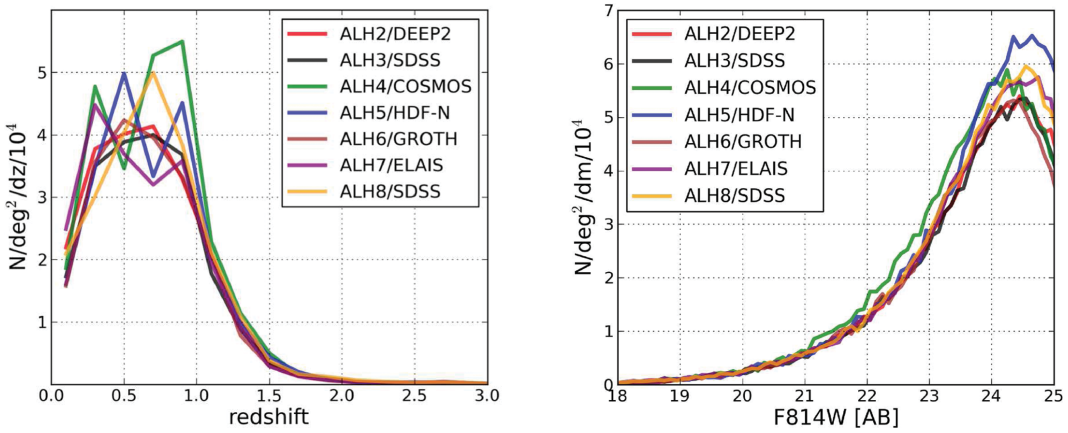

Figure 33. Effect of the cosmic variance on $P(z)$. The left panel shows the redshift probability distribution function $P(z)$ for all the seven ALHAMBRA fields, using a range of magnitudes $19.0 < m_{F814W} < 23.5$. The different ALHAMBRA fields are colour-coded as indicated in the legend. Once again, the ALHAMBRA-04 field associated with the COSMOS fields (green line) shows a peculiar distribution with a prominent peak at redshift $z \sim 0.86$. The right panel shows the cumulative number counts for the seven fields. Again, the ALHAMBRA-4 field (green line) shows a clear excess in the number of galaxies detected per magnitude range with respect to the other fields.

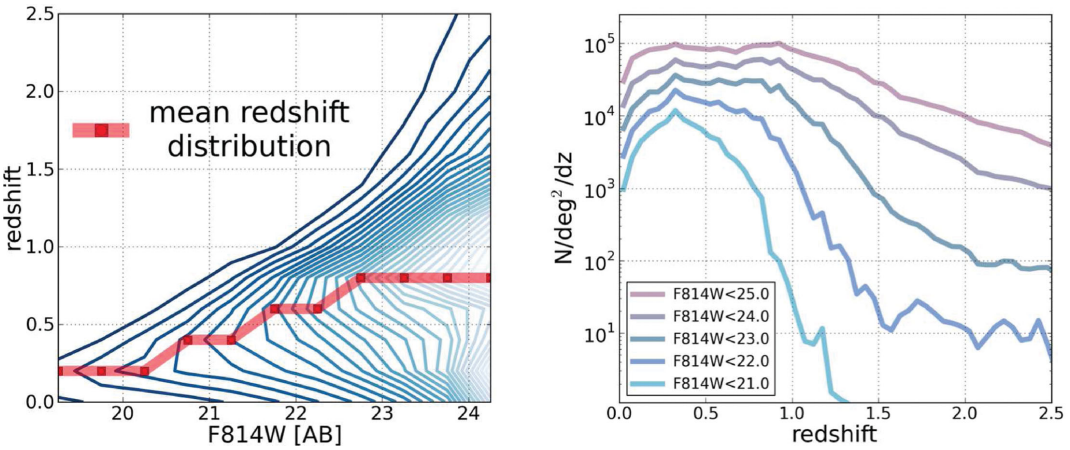

Figure 34. Evolution of the redshift distribution. The left panel shows the evolution of the averaged redshift distribution for the ALHAMBRA fields, as a function of the magnitude $F814W$. The mean redshift distribution (solid red line) indicates a clear evolution moving from $\langle z \rangle \sim 0.2$ for $m_{F814W} < 20.5$ to $\langle z \rangle \sim 0.86$ for $m_{F814W} > 23.0$. The right panel shows the averaged distribution of galaxies for the ALHAMBRA fields, as a function of redshift for different ranges in magnitude.

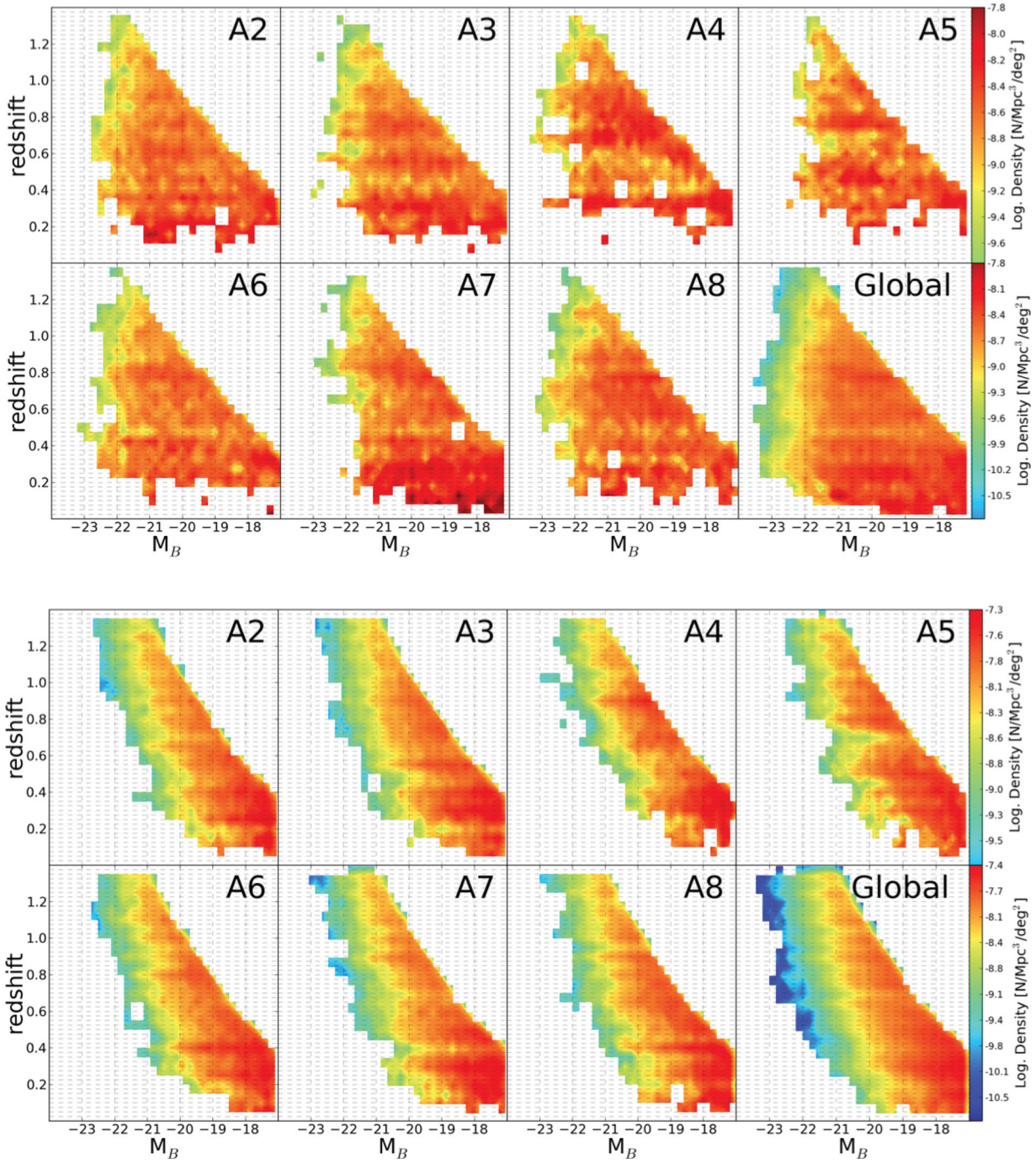

Figure 35. Redshift distribution in the rest frame per ALHAMBRA field. We explored the variance in the redshift–magnitude distribution of galaxies as a function of the absolute B magnitude and spectral type. After splitting the sample into early-type galaxies (top panel, defined as $1 < T_b < 5$) and late-type galaxies (bottom panel, defined as $7 < T_b < 11$), we compared the resulting distributions among the seven individual ALHAMBRA fields (A_i) + one averaged sample (*Global*). As observed from the panels, where the logarithmic density is colour-coded, whereas each individual field shows clear and identifiable structures at different redshifts, the global samples show a more smooth distribution. In particular, we find that the well-known bimodal distribution in the COSMOS field (A4) is not systematically observed along the other fields, emphasizing the effects of cosmic variance on galaxy evolution studies.

4.4 Photometric redshift depth

Due to the colour/redshift degeneracies, it is possible to have galaxies that are detected at high S/N in many filters but for which no unambiguous redshifts can be derived. One of the main practical ways of characterizing the effective completeness and depth of a photometric redshift catalogue is by using the number of galaxies with *Odds* above a certain threshold, which basically tells us how many galaxies we can expect to have with meaningful, unambiguous photometric redshifts (Benítez 2000; Benítez et al. 2009b).

We therefore took into account *Odds* to carry out a set of analyses and evaluate the completeness and accuracy of our sample. For this, we set the interval to compute the *Odds* parameter to $DZ = 2 \times 0.0125 \times (1 + z)$, since this quantity corresponds to

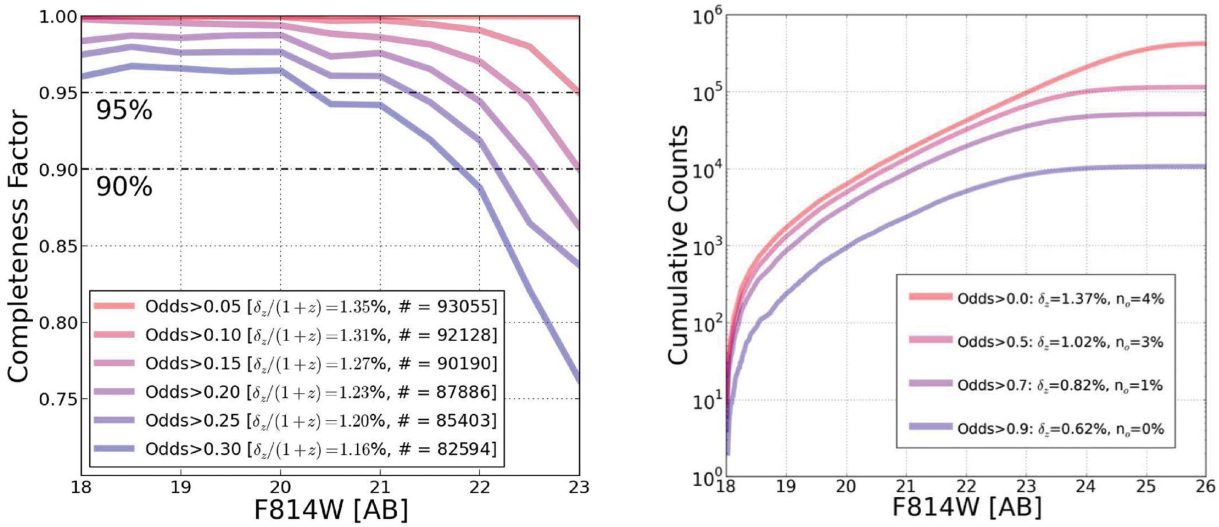

Figure 36. Photometric redshift depth. In order to characterize the photometric redshift depth for the ALHAMBRA catalogues, we quantified the number of galaxies per *Odds* interval, which is equivalent to estimating the fraction and distribution of galaxies with a certain expected photometric redshift accuracy. As seen in the left panel, we explored the expected completeness factor as a function of the magnitude *F*814*W* and *Odds* interval. The total fraction of galaxies within each interval is specified in the legend. Similarly, the right panel shows the cumulative distribution of galaxies as a function of the *F*814*W* magnitude for different *Odds* intervals. The expected accuracy for photometric redshift δ_z and the fraction of catastrophic outliers n_o (according to the spectroscopic sample) are indicated in the legend.

twice the expected σ. The completeness factor (fraction of galaxies per *Odds* interval) as a function of *F*814*W* magnitude is presented in Fig. 36.

For sources detected only in the *F*814*W* detection image, an upper limit (defined as 1σ above the background) is provided. These limiting magnitudes represent the deepest magnitudes extractable from an image, providing useful information for the SED-fitting analysis. Limiting magnitudes are applied whenever measured fluxes, inside a fixed aperture, are equal to or lower than the estimation of the background signal. Since limiting magnitudes depend directly on photometric errors, we computed limiting magnitudes after re-estimating photometric errors, via empirical sigma estimation (Section 3.7). Derived limiting magnitudes for each band can be found within the photometric catalogues. In Fig. 37, we represent the averaged 5σ limiting magnitudes for all 23 bands using fixed circular apertures of 3 arcsec.

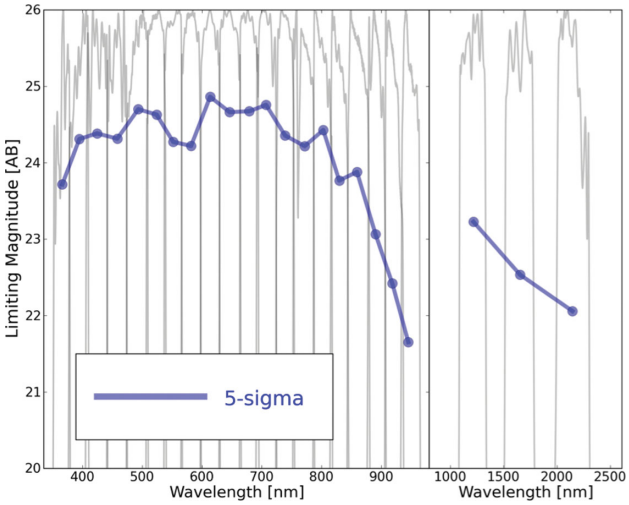

Figure 37. Limiting magnitudes. We derived limiting magnitudes for every image, as they represent a very useful piece of information during the SED-fitting procedure. As required by BPZ, we replaced galaxies with measured fluxes equal to or lower than the estimation of the background signal by an upper limit defined as 1σ above the background. Since limiting magnitudes depend on the photometric uncertainties, we computed limiting magnitudes after re-estimating the photometric errors empirically. Meanwhile, we calculated the expected limiting magnitude using fixed apertures of 3 arcsec and 5σ, as seen in the figure. These magnitudes correspond to the averaged values for the complete set of images.

4.5 Emission-line galaxies

When plotting the *Odds* distribution as a function of *F*814*W* magnitude for all galaxies (Fig. 38), we find a concentration of objects with low odds at magnitudes between $18 < m_{F814W} < 23$ and $0.0 < Odds < 0.1$. When plotting the logarithmic χ^2 distribution for those objects, it immediately reveals those detections to have very high χ^2 values (since BPZ.2 will automatically assign low odds to those objects) indicative of a poor fit, as the right panel in Fig. 38 illustrates.

Detections with unexpected poor χ^2 fitting (given its magnitude) could be due to incorrect photometry or to an incomplete library of templates. After purging the sample from objects with high SExtractor flags, we saw that the remaining galaxies in that locus could be classified into two different groups: (1) unresolved stellar pairs (identified as a single detection by SExtractor) with clearly asymmetric morphologies (despite their photometric colours) and (2) very strong broad emission-line objects. As mentioned in Section 4, neither AGN nor QSO templates were included in the BPZ library and therefore these sources might be expected to show poor fits to any BPZ template. In fact, this is a good way of finding active galaxies, as illustrated in the left panel of Fig. 38. Given the high value of χ^2, the new version of BPZ generates for them a redshift distribution that is (in most cases) assigned by the prior probability,

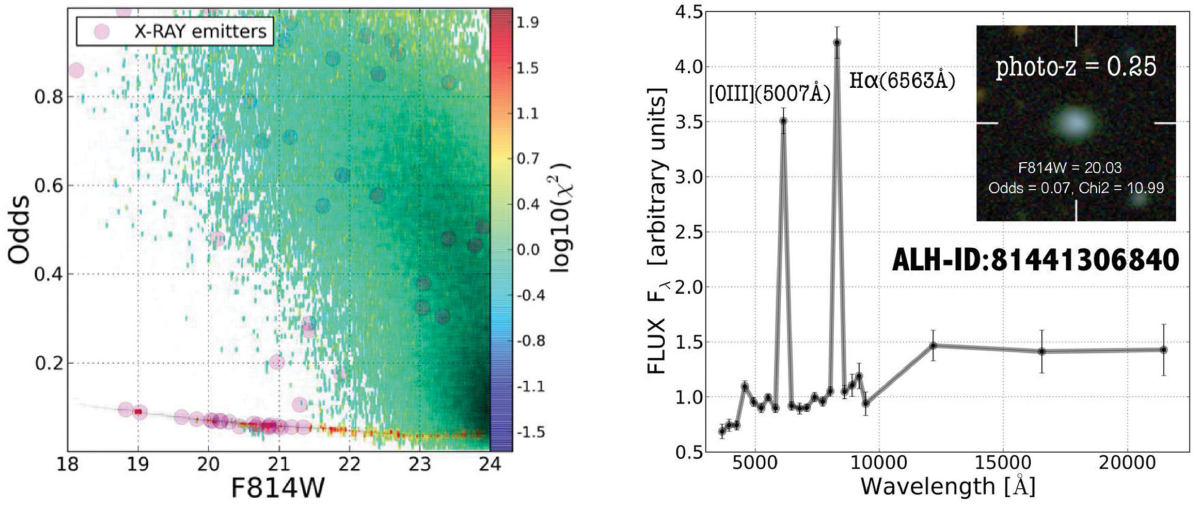

Figure 38. Emission-line galaxy identification. The left panel shows the *Odds* distribution as a function of magnitude *F*814*W* for the complete catalogue (stars excluded). As expected, there is a clear dependence between *Odds* and magnitude, indicating how the photometric redshift confidence decreases with S/N. We observed an unexpected locus for magnitudes in range $18 < m_{F814W} < 24$ and *Odds* in range $0.0 < Odds < 0.1$. When plotting the logarithmic χ^2 distribution, it revealed those detections to have extremely high χ^2 values when SED-fitting the BPZ galaxy templates. We observed that those sources were mostly composed of very strong broad emission-line objects, AGNs and QSOs, galaxy types not included in the BPZ library of templates. The right panel shows an example of an intense emission-line galaxy within that horizontal sequence.

favouring solutions near the prior mode $z_b \sim 0.4$ for intermediate spectral types T_b (E0/Scd/Sbc).

5 PHOTOMETRIC CATALOGUES

As explained in Section 3.5, we have generated homogeneous *F*814*W*-based catalogues across ∼3.0 deg^2, combining the available information from our 23 + 1 photometric filters. The full area is then divided into 48 individual catalogues containing the information listed in Appendix C1 and C2.

Unique IDs are given to every detection according to the following criteria: ID = 81442100119 stands for 814 (detection image) + 4 (field) + 2 (pointing) + 1 (CCD) + 00119 (ColorPro_ID). Both astrometric and geometrical information are therefore derived from the corresponding *F*814*W* detection image: f04p02_F814W_1.swp.fits (following the former example). SExtractor detection parameters were chosen differently for every detection image, as discussed in Section 3.5.2. Kron apertures (RK) and fraction-of-light radii (RF) were settled according to the aperture parameters defined in Table D1. Total magnitudes and empirically corrected uncertainties (Section 3.7) are given by all 24 filters. Along with this, F814W_3arc represents *F*814*W* magnitudes measured on a 3-arcsec circular apertures and likewise F814W_3arc_corr, but corrected to match COSMOS/*F*814*W* photometry (Section 3.5). As every detection in the ALHAMBRA fields was covered by all 24 filters, *nfd* indicates the number of filters in which a source was detected. Whenever a source was not detected, its magnitude was set to 99. and its photometric uncertainty replaced by a 1σ upper limit (Section 4.4) suitable for BPZ.

The final catalogues contain several quality flags. *PhotoFlag* corresponds to the standard SExtractor photometric flag (Bertin & Arnouts 1996), *Satur_Flag* indicates a possible saturated source (typically stars with magnitudes brighter than $m_{F814W} = 16$), *Stellar_Flag* represents a source-by-source statistical classification among stars and galaxies (Section 3.6) and *irms_OPT_Flag* and *irms_NIR_Flag* indicate the number of optical and NIR bands in which a detection was observed with a normalized exposure time below 80 per cent, respectively. The *DupliDet_Flag* indicates that a source was detected twice (within the overlapping area among consecutive detectors). If so, the detection with the poorest S/N is set to a value *DupliDet_Flag* = 1. Therefore, selecting detections with *DupliDet_Flag* = 0 removes all duplicated detections when combining catalogues.

The best photometric redshift estimate for every source is z_b. Additionally, z_b^{min} and z_b^{max} represent the lower and upper limits for the first peak within a 1σ interval. Spectral type classification is given by T_b, where its number refers to the selected template as indicated in Fig. 21. *Odds* gives the amount of redshift probability enclosed around the main peak (see Section 4) and χ^2 is the reduced squared chi from the comparison between observed and predicted fluxes according to the selected template and redshift. An estimation of each detection stellar mass content (in units of $\log_{10}(M_\odot)$) is given by *Stell_Mass*. *M_ABS* corresponds to the absolute (AB) magnitude for the Johnson *B* band (Johnson & Morgan 1953). *MagPrior* corresponds to the *F*814*W* magnitude used to derived the BPZ prior. Finally, z_{ml} and t_{ml} represent respectively the maximum-likelihood photometric redshift and spectral type.

6 THE ALHAMBRA 'GOLD' CATALOGUE

The ALHAMBRA gold catalogue corresponds to a subsample of ∼100k galaxies ($17 < m_{F814W} < 23$) with very accurate and reliable photometric redshifts, an expected error $\sigma_z < 0.012$ and redshift probability distribution functions $P(z)$ well-defined by a single peak. The catalogue also includes PSF-corrected photometry for ∼20 000 stars in the Galactic halo (identified according to the methodology described in Section 3.6), along with ∼1000 AGN candidates found with the method discussed in Section 4.5.

The ALHAMBRA gold catalogue can be downloaded from the website http://cosmo.iaa.es/content/alhambra-gold-catalog.

7 SUMMARY

The ALHAMBRA survey has observed eight different regions of the sky, including sections of the COSMOS, DEEP2, ELAIS, GOODS-N, SDSS and Groth fields, using a new photometric system with 20 contiguous ∼300 Å filters covering the optical range and combining them with deep *JHKs* imaging. The observations, carried out with the Calar Alto 3.5-m telescope using the wide-field (0.25 deg^2 FOV) optical camera LAICA and the NIR instrument Omega-2000, correspond to ∼700 h of on-target science images. The photometric system was specifically designed to maximize the effective depth of the survey in terms of accurate spectral type and photometric redshift estimation, along with the capability for identification of relatively faint emission lines.

Synthetic *HST*/ACS *F*814*W* detection images were generated in order to define a constant and homogeneous window for all the ALHAMBRA fields. These images, photometrically complete down to a magnitude $m_{F814W} \leq 25.5$ AB, served not only to improve the quality of the photometric detections but also to carry out systematic comparisons with the COSMOS survey. In order to improve the source detection efficiency, we masked every saturated star, stellar spike, ghost and damaged area. To minimize the variation of the image RMS, all flagged pixels were replaced with background noise.

To deal with the observed PSF variability across filters, ColorPro (Coe et al. 2006) was used to perform accurate aperture-matched PSF-corrected photometry, retrieving robust photometric colours ideal for photometric redshift estimations. For this purpose, PSF models were generated for individual images by manually selecting several hundred non-saturated and well-isolated stars across the field. Using a compilation of ∼20 000 stars, the mean radial PSF variation was smaller than 5 per cent, enabling the usage of a single PSF model per image.

We carried out several simulations to test the accuracy of ColorPro in retrieving precise photometry across images with varied PSF. We degraded ACS/*HST* images (from COSMOS) to the typical ALHAMBRA conditions (in terms of PSF and background noise) and ran ColorPro on these, expecting to retrieve null colours (equal magnitudes). We found that simulated colours showed a dispersion of $\sigma \sim 0.03$, which marks a photometric precision floor for sources brighter than magnitude $m_{F814W} = 23.0$, and, as expected from the uncertainties arising from the photometric noise, an increasing error for fainter magnitudes. For most of the magnitude range, there are negligible biases.

We also studied the expected photometric completeness for the ALHAMBRA fields in terms of the PSF and background level, using the previous simulations. We therefore derived the statistical probability of detecting a sample of faint galaxies when observed under typical ALHAMBRA conditions. The result indicates that ALHAMBRA is photometrically complete down to a magnitude of $m_{F814W} \sim 24$. At fainter magnitudes, the number of detections decreases rapidly, with ∼40 per cent of the galaxies lost at $m_{F814W} \sim 25$.

To decontaminate extragalactic sources from field stars, we followed a statistical approach where every detection was classified in terms of the probability of being a star or a galaxy, given its apparent geometry, *F*814*W* magnitude, optical $F489W - F814W$ and NIR $J - Ks$ colours. We tested the goodness of our statistical classification by comparing the density of finding stars against that predicted by the Trilegal software (Girardi et al. 2002, 2005). We found very good agreement between both samples. When this statistical criterion is applied to the complete catalogue, we observed that stars dominate the sample down to a magnitude $m_{F814W} < 19$. For fainter magnitudes, the fraction of stars rapidly declines, with a contribution of ∼1 per cent for magnitudes $m_{F814W} = 22.5$. We retrieve an averaged stellar density in the galactic halo of ∼7000 stars per deg^2 (∼450 stars per CCD) for sources brighter than $m_{F814W} = 22.5$.

Given the correlation among pixels introduced during image processing, we empirically recalculated photometric uncertainties for every detection, following a similar approach to that described in Labbé et al. (2003), Gawiser et al. (2006) and Quadri et al. (2007). Spanning a range of radius between 1 and 250 pixels, we drawn ∼50 000 apertures on blank areas across the images to measure both the enclosed background signal and its scatter. The methodology served to estimate properly the empirical dependence between any galaxy photometric aperture and its photometric uncertainty.

We calculated photometric redshifts with the bpz2.0 code (Benítez, in preparation). This new version includes a new prior empirically derived for each spectral type and magnitude by fitting luminosity functions provided by GOODS- MUSIC (Santini et al. 2009), COSMOS (Scoville et al. 2007) and UDF (Coe et al.2006), a new empirically calibrated library of galaxy templates and an estimation of the galaxy stellar mass based on the colour–M/L ratio relationship established by Taylor et al. (2011).

Given the overlap between ALHAMBRA fields and other existing spectroscopic surveys, we compiled a sample of ∼7200 galaxies with high-quality (secure) spectroscopic redshifts from the publicly available data, mostly covering the ALHAMBRA parameter space, i.e. with a redshift range $0 < z_s < 1.5$ ($\langle z_s \rangle \sim 0.77$) and a magnitude range (based on ALHAMBRA photometry) $18 < m_{F814W} < 25$ ($\langle m_{F814W} \rangle \sim 22.3$). Based on this spectroscopic sample, our photometric redshifts have a precision of $\delta_z/(1 + z_s) = 1$ per cent for $I < 22.5$ and $\delta_z/(1 + z_s) = 1.4$ per cent for $22.5 < I < 24.5$. Precisions of $\delta_z/(1 + z_s) < 0.5$ per cent are reached for the brighter spectroscopic sample, showing the potential of medium-band photometric surveys.

We refined photometric zero-points derived using standard stellar-based calibration techniques, by comparing the observed colours of galaxies (for which spectroscopic redshifts were available) with those expected by the bpz library of templates. We found that the corrections thus derived not only improved the photometric redshift accuracy but also reduced the fraction of catastrophic outliers. Considering the possibility of a systematic effect during the data reduction, we represented the zero-point corrections globally for all individual images as a function of AIRMASS, stellar symmetry, FWHM scatter, differences between PSF models and stars, magnitude ranges, redshift ranges or aperture sizes. No clear correlations were observed, with typical fluctuations smaller than 3 per cent. We therefore conclude that the zero-point offsets do not depend on the photometric treatment and represent real differences between the calibration obtained from traditional colour transformations based on stars and the average colours of galaxies as defined by the bpz template set, calibrated with *HST* observations.

For those fields without spectroscopic coverage, a new methodology (described in this work) was applied to calibrate photometric zero-point estimations using photometric redshifts. Essentially, we realized that the photometric redshifts obtained for emission-line galaxies were quite robust to changes in the zero-point calibration and therefore could be treated as spectroscopic for calibration purposes, obtaining an automatic and self-contained zero-point correction for all our fields. This methodology not only successfully improved the photometric redshift accuracy (almost up to the level provided by the spectroscopic sample), but also dramatically

reduced the fraction of catastrophic outliers, avoiding the serious problem of inhomogeneity among fields.

Considering the probabilistic nature of the photometric redshift estimations, we worked with the full probability distribution $P(z, T|C)$ (Benítez 2000; Coe et al. 2006; Mandelbaum et al. 2008; Cunha et al. 2009; Wittman 2009; Bordoloi et al. 2010; Abrahamse et al. 2011; Sheldon et al. 2012). This approach represents a more convenient estimator for most faint galaxies, as $p(z)$ usually becomes multimodal and completely asymmetric, so is not well represented by a single and symmetric distribution. Using the complete probability distribution functions, we found that the global photometric redshift distribution shows a mean redshift $\langle z\rangle = 0.56$ for $I < 22.5$ AB and $\langle z\rangle = 0.86$ for $I < 24.5$ AB. In particular, comparison with our average $n(z)$ shows that the COSMOS field has a rather peculiar redshift distribution, with a large spike at $z \sim 0.7$ and an underdensity for $z < 0.5$, which mimics a significant redshift density evolution effect.

Despite having a relatively small FOV compared with other surveys, one of the main virtues of ALHAMBRA is that it includes eight different lines of sight widely separated, providing a realistic estimation of both the typical redshift distribution of galaxies across cosmic time and its inherent variability. We explored the cosmic variance effect in the redshift distribution of galaxies as a function of absolute B magnitude and spectral type. We found that the well-known bimodal distribution in the COSMOS field was not systematically observed along the other fields, emphasizing the usefulness of the ALHAMBRA data in galaxy evolution studies.

We discovered a new methodology to identify potential AGN candidates using BPZ. When plotting the *Odds* distribution as a function of $F814W$ magnitude for all galaxies, we found a concentration of objects with low *Odds* at magnitudes in range $18 < m_{F814W} < 23$. When plotting the logarithmic χ^2 distribution for these objects, it immediately revealed those detections to have the highest χ^2 values, indicative of a poor fit. After purging the sample of objects with high SExtractor flags, we saw that the remaining objects could be classified into two different groups: (1) unresolved stellar pairs with clearly asymmetric morphologies (in spite of their photometric colours) and (2) very strong broad emission-line objects, AGNs or variable sources. These are precisely the templates not included in the BPZ library.

The PSF-corrected multicolour photometry and photometric redshifts for ∼438 000 galaxies presented in this work cover an effective area of 2.79 deg^2, split into 14 strips of 58.5 × 15.5 arcmin^2, and represent ∼32 h of on-target exposure time. Given its depth, multiband coverage and much smaller cosmic variance than other similar projects, ALHAMBRA is a unique data set for galaxy evolution studies. Several of the techniques presented here will have wide applicability to future large-scale narrow-band photometric redshift surveys like JPAS (Benítez et al. 2009a; Benítez, in preparation).

ACKNOWLEDGEMENTS

We acknowledge support from the Spanish Ministerio de Educación y Ciencia through grant AYA2006-14056 BES-2007-16280. We acknowledge financial support from the Spanish MICINN under the Consolider-Ingenio 2010 Program grant CSD2006-00070: First Science with the GTC. Part of this work was supported by Junta de Andalucía, through grant TIC-114 and the Excellence Project P08-TIC-3531, and by the Spanish Ministry for Science and Innovation through grants AYA2006-1456, AYA2010-15169, AYA2010-22111-C03-02, AYA2010-22111-C03-01 and Generalitat Valenciana project Prometeo 2009/064. Based on observations collected at the Centro Astronómico Hispano Alemán (CAHA) at Calar Alto, operated jointly by the Max-Planck Institut für Astronomie and the Instituto de Astrofísica de Andalucía (IAA–CSIC).

REFERENCES

Abrahamse A., Knox L., Schmidt S., Thorman P., Tyson J. A., Zhan H., 2011, ApJ, 734, 36
Aparicio-Villegas T. et al., 2010, AJ, 139, 1242
Baum W. A., 1962, in McVittie G., ed., IAU Symp. 15, Problems of Extra-Galactic Research. Macmillan Press, New York, p. 390
Benítez N., 2000, ApJ, 536, 571
Benítez N. et al., 2004, ApJ, 150, 1
Benítez N. et al., 2009a, ApJL, 692, 5B
Benítez N. et al., 2009b, ApJ, 691, 241
Benítez N. et al., 2014, preprint (arXiv:1403.5237)
Bernardi M. et al., 2010, MNRAS, 404, 2087
Bertin E., Arnouts S., 1996, A&A, 117, 393
Bertin E., Mellier Y., Radovich M., Missonnier G., Didelon P., Morin B., 2002, Astronomical Data Analysis Software and Systems XI, 281, 228
Bohlin R. C., 2007, The Future of Photometric, Spectrophotometric and Polarimetric Standardization, 364, 315
Bongiovanni A. et al., 2010, A&A, 519, L4
Bordoloi R., Lilly S. J., Amara A., 2010, MNRAS, 406, 881
Brammer G. B., van Dokkum P. G., Coppi P., 2008, ApJ, 686, 1503
Bundy K. et al., 2006, ApJ, 651, 120
Capak P. et al., 2007, ApJS, 172, 99
Cardamone C. N. et al., 2010, ApJS, 189, 270
Casertano S. et al., 2000, AJ, 120, 2747
Coe D., Benítez N., Sánchez S. F., Jee M., Bouwens R., Ford H., 2006, AJ, 132, 926
Cristóbal-Hornillos D. et al., 2009, ApJ, 696, 1554
Csabai I. et al., 2003, AJ, 125, 580
Cunha C. E., Lima M., Oyaizu H., Frieman J., Lin H., 2009, MNRAS, 396, 2379
Cutri R. M. et al., 2003, 2MASS All Sky Catalog of point sources. NASA/IPAC Infrared Science Archive
Daddi E., Cimatti A., Renzini A., Fontana A., Mignoli M., Pozzetti L., Tozzi P., Zamorani G., 2004, ApJ, 617, 746
Dahlen T. et al., 2010, ApJ, 724, 425
Davis M. et al., 2007, ApJL, 660, L1
de Santis C., Grazian A., Fontana A., Santini P., 2007, New Astron., 12, 271
Fernández-Soto A., Lanzetta K. M., Yahil A., 1999, ApJ, 513, 34
Fernández-Soto A., Lanzetta K. M., Chen H.-W., Pascarelle S. M., Yahata N., 2001, ApJS, 135, 41
Fioc M., Rocca-Volmerange B., 1997, A&A, 326, 950
Gawiser E. et al., 2006, ApJS, 162, 1
Girardi L., Bertelli G., Bressan A., Chiosi C., Groenewegen M. A. T., Marigo P., Salasnich B., Weiss A., 2002, A&A, 391, 195
Girardi L., Groenewegen M. A. T., Hatziminaoglou E., da Costa L., 2005, A&A, 436, 895
Gregg M. D. et al., 2004, BAAS, 36, 1496
Hickson P., Mulrooney M. K., 1998, ApJS, 115, 35
Hildebrandt H., Wolf C., Benítez N., 2008, A&A, 480, 703
Ilbert O. et al., 2006, A&A, 457, 841
Ilbert O. et al., 2009, ApJ, 690, 1236
Johnson H. L., Morgan W. W., 1953, ApJ, 117, 313
Kuijken K., 2008, A&A, 482, 1053
Labbé I. et al., 2003, AJ, 125, 1107
Laidler V. G. et al., 2006, Astronomical Data Analysis Software and Systems XV, 351, 228
Lanzetta K. M., Yahil A., Fernández-Soto A., 1996, Nature, 381, 759
Lilly S. J. et al., 2009, ApJS, 184, 218
Loh E. D., Spillar E. J., 1986, ApJ, 303, 154
Madau P., 1995, QSO Absorption Lines, 377
Mandelbaum R. et al., 2008, MNRAS, 386, 781

Matute I. et al., 2012, A&A, 542, A20
Matute I. et al., 2013, A&A, 557, A78
Merson A. I. et al., 2013, MNRAS, 429, 556
Mitchell P. D., Lacey C. G., Baugh C. M., Cole S., 2013, MNRAS, 435, 87
Moles M. et al., 2008, AJ, 136, 1325
Pérez-González P. G. et al., 2013, ApJ, 762, 46
Quadri R. et al., 2007, AJ, 134, 1103
Rowan-Robinson M. et al., 2008, MNRAS, 386, 697
Santini P. et al., 2009, VizieR Online Data Catalog, 350, 40751
Sawicki M. J., Lin H., Yee H. K. C., 1997, AJ, 113, 1
Scoville N. et al., 2007, ApJS, 172, 38
Sheldon E. S., Cunha C. E., Mandelbaum R., Brinkmann J., Weaver B. A., 2012, ApJS, 201, 32
Stetson P. B., 1987, PASP, 99, 191
Taniguchi Y. et al., 2005, J. Korean Astron. Soc., 38, 187
Taylor E. N. et al., 2011, MNRAS, 418, 1587
Tucker D. L., Smith J. A., Brinkmann J., 2001, in Clowes R., Adamson A., Bromage G., eds ASP Conf. Ser. Vol. 232, The New Era of Wide Field Astronomy. Astron. Soc. Pac., San Francisco, p. 13
van Dokkum P. G. et al., 2009, PASP, 121, 2
Watson M. G. et al., 2009, A&A, 493, 339
Williams R. E. et al., 1996, AJ, 112, 1335
Wittman D., 2009, ApJ, 700, L174
Wolf C. et al., 2001a, A&A, 365, 681
Wolf C., Meisenheimer K., Roser H.-J., 2001b, A&A, 365, 660
Wolf C., Hildebrandt H., Taylor E. N., Meisenheimer K., 2008, A&A, 492, 933
Wuyts S., Labbé I., Schreiber N. M. F., Franx M., Rudnick G., Brammer G. B., van Dokkum P. G., 2008, ApJ, 682, 985
York D. G. et al., 2000, AJ, 120, 1579

APPENDIX A: THE ALHAMBRA FIELDS NOMENCLATURE

In Fig. A1, we illustrate an example of the Pointing layout for the ALHAMBRA fields. The combination of two contiguous pointings yields a final layout composed of two strips of 58.5 × 15.5 arcmin^2 (comprising four individual CCDs) with a separation of ∼13.0 arcmin.

APPENDIX B: PHOTOMETRIC REDSHIFT SURVEY COMPARISON

Fig. B1 represents the photometric redshift accuracy versus the covered area for several surveys (see Table 2). The number of photometric passbands is colour-coded as described in the inset panel. The marker size represents the number of detections logarithmically.

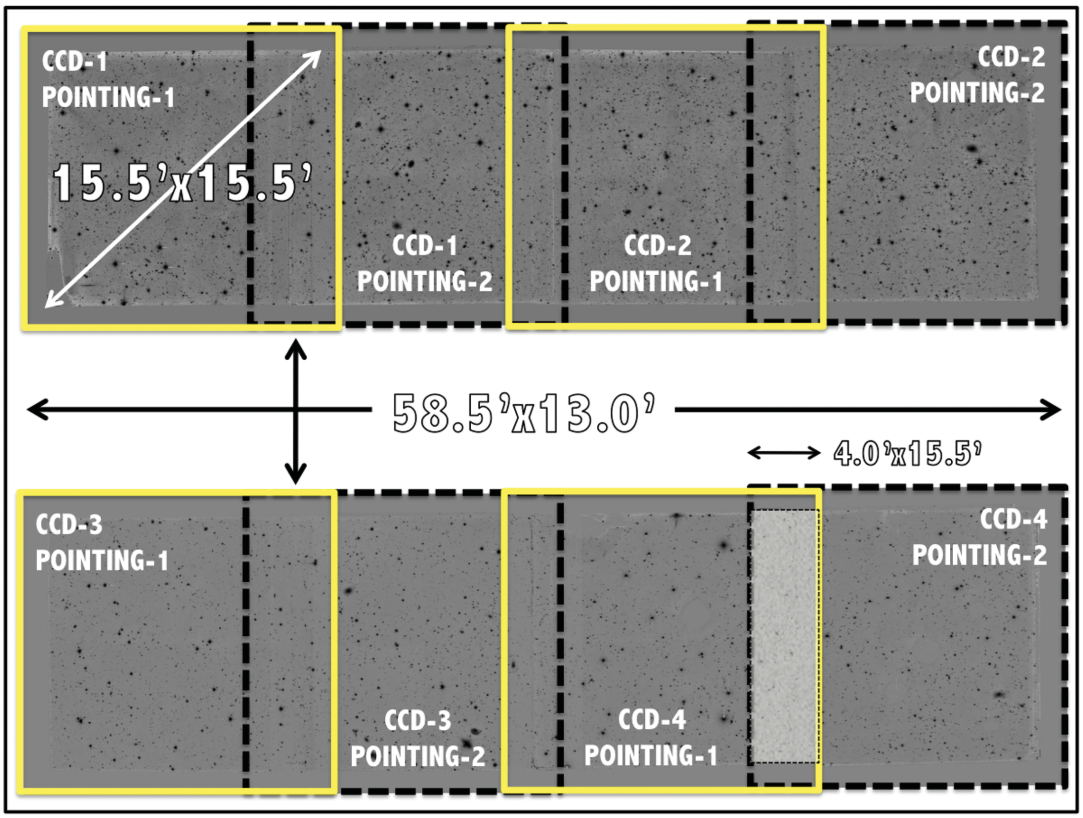

Figure A1. Pointing layout for the ALHAMBRA fields. Given the geometrical configuration of the optical imager LAICA, each pointing is composed of four CCDs (as marked with the yellow squares) with an internal gap of ∼13.0 arcmin. The combination of two contiguous pointings yields a final layout composed of two strips of 58.5 × 15.5 arcmin^2 (comprising four individual CCDs) with a separation of ∼13.0 arcmin. Contiguous CCDs within each strip show a maximum overlap of 4.0 × 15.5 arcmin^2.

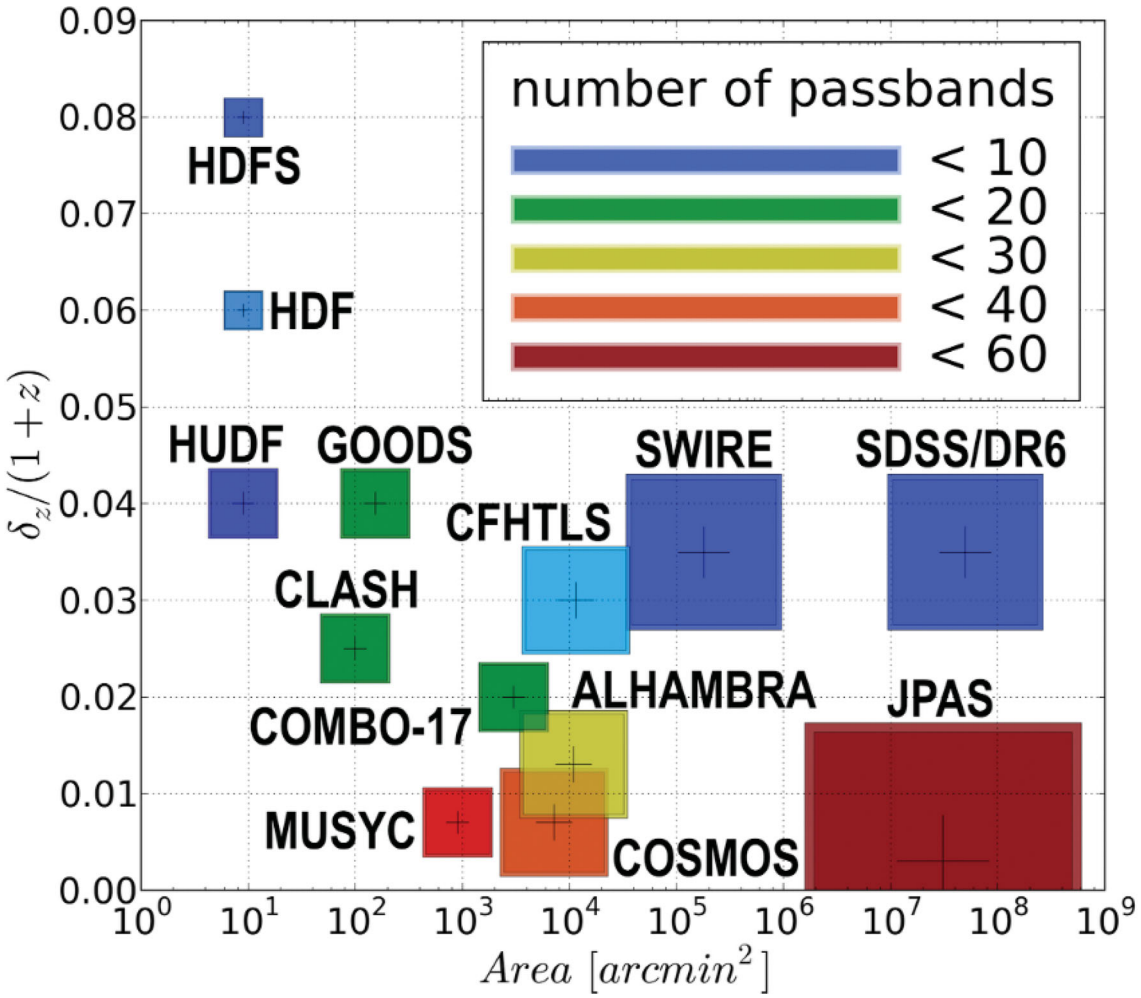

Figure B1. Photometric redshift survey comparison. The figure represents the photometric redshift accuracy versus the covered area for several surveys (see Table 2). The number of photometric passbands is colour-coded as described in the inset panel. The marker size represents the number of detections logarithmically, while the position of the internal plus sign indicates its photometric redshift accuracy.

APPENDIX C: PHOTOMETRIC REDSHIFT CATALOGUE DESCRIPTION

In Table C1, we include a description of the photometric redshift catalogue content in more detail.

APPENDIX D: SEXTRACTOR CONFIGURATION AND THE EFFECTIVE AREA

In Table D1, we present an example of the SExtractor configuration used to derive the *F*814*W* detections. Along with this, we also include another table (Table D2) containing statistical information concerning the observations.

Table C1. ALHAMBRA photometric redshift catalogue content.

Column	Parameter	Description
1	ID_ColorPro	Object ID number
2	Field	ALHAMBRA field
3	Pointing	Pointing within the field
4	CCD	Detector within the pointing
5	RA	Right Ascension in decimal degrees [J2000]
6	DEC	Declination in decimal degrees [J2000]
7	XX	x pixel coordinate
8	YY	y pixel coordinate
9	AREA	Isophotal aperture area (pixels)
10	FWHM	Full width at half-maximum (arcsec)
11	STELL	SExtractor 'stellarity' (1 = star; 0 = galaxy)
12	ELL	Ellipticity $= 1 - B/A$
13	a	Profile RMS along major axis (pixels)
14	b	Profile RMS along minor axis (pixels)
15	THETA	Position Angle (CCW/x)
16	RK	Kron apertures in units of A or B (pixels)
17	RF	Fraction-of-light radii (pixels)
18	S/N	Signal-to-noise ratio (SExt_FLUX_AUTO/SExt_FLUXERR_AUTO)
19	PhotoFlag	SExtractor Photometric Flag
20,21	F365W, dF365W	$F365W$ total magnitude & uncertainty
22,23	F396W, dF396W	$F396W$ total magnitude & uncertainty
24,25	F427W, dF427W	$F427W$ total magnitude & uncertainty
26,27	F458W, dF458W	$F458W$ total magnitude & uncertainty
28,29	F489W, dF489W	$F489W$ total magnitude & uncertainty
30,31	F520W, dF520W	$F520W$ total magnitude & uncertainty
32,33	F551W, dF551W	$F551W$ total magnitude & uncertainty
34,35	F582W, dF582W	$F582W$ total magnitude & uncertainty
36,37	F613W, dF613W	$F613W$ total magnitude & uncertainty
38,39	F644W, dF644W	$F644W$ total magnitude & uncertainty
40,41	F675W, dF675W	$F675W$ total magnitude & uncertainty
42,43	F706W, dF706W	$F706W$ total magnitude & uncertainty
44,45	F737W, dF737W	$F737W$ total magnitude & uncertainty
46,47	F768W, dF768W	$F768W$ total magnitude & uncertainty
48,49	F799W, dF799W	$F799W$ total magnitude & uncertainty
50,51	F830W, dF830W	$F830W$ total magnitude & uncertainty
52,53	F861W, dF861W	$F861W$ total magnitude & uncertainty
54,55	F892W, dF892W	$F892W$ total magnitude & uncertainty
56,57	F923W, dF923W	$F923W$ total magnitude & uncertainty
58,59	F954W, dF954W	$F954W$ total magnitude & uncertainty
60,61	J, dJ	NIR-J total magnitude & uncertainty
62,63	H, dH	NIR-H total magnitude & uncertainty
64,65	KS, dKS	NIR-KS total magnitude & uncertainty
66,67	F814W, dF814W	$F814W$ total magnitude & uncertainty
68	F814W_3arcs	3 arcsec Circular Aperture magnitude [AB]
69	dF814W_3arcs	3 arcsec Circular Aperture magnitude uncertainty [AB]
70	F814W_3arcs_corr	Corrected 3 arcsec Circular Aperture magnitude [AB]
71	nfd	Number filters detected (out of 24)
72	xray	X-ray source [0:NO,1:YES] (2XMM;Watson et al. 2009)
73	PercW	Percentual Photometric weight (on detection image).
74	Satur_Flag	Photometric saturation flag [0:Good Detection, 1:Saturated Detection]
75	Stellar_Flag	Statistical STAR/GALAXY discriminator [0:Galaxy,0.5:Unknown,1:Star]
76	DupliDet_Flag	Duplicated detection flag [0:Non duplicated, 1:Duplicated]
77	zb	BPZ most likely redshift
78	zb_min	Lower limit (95p confidence)
79	zb_max	Upper limit (95p confidence)
80	T_b	BPZ most likely spectral type
81	Odds	$P(z)$ contained within zb +/− 2*0.01*(1+z)
82	z_ml	Maximum-likelihood most likely redshift
83	t_ml	Maximum-likelihood most likely spectral type
84	Chi2	Poorness of BPZ fit: observed versus model fluxes
85	Stell_Mass	Stellar mass ($\log_{10}(M_{\odot})$)
86	M_ABS	Absolute magnitude [AB] (B_JOHNSON)
87	MagPrior	Magnitude used for the prior (F814W)
88	irms_F365W	Percentual weight on F365W 1/RMS image (within ISOphotal Area).

Table C1 – *continued*

Column	Parameter	Description
89	irms_F396W	Percentual weight on F396W 1/RMS image (within ISOphotal Area).
90	irms_F427W	Percentual weight on F427W 1/RMS image (within ISOphotal Area).
91	irms_F458W	Percentual weight on F458W 1/RMS image (within ISOphotal Area).
92	irms_F489W	Percentual weight on F489W 1/RMS image (within ISOphotal Area).
93	irms_F520W	Percentual weight on F520W 1/RMS image (within ISOphotal Area).
94	irms_F551W	Percentual weight on F551W 1/RMS image (within ISOphotal Area).
95	irms_F582W	Percentual weight on F582W 1/RMS image (within ISOphotal Area).
96	irms_F613W	Percentual weight on F613W 1/RMS image (within ISOphotal Area).
97	irms_F644W	Percentual weight on F644W 1/RMS image (within ISOphotal Area).
98	irms_F675W	Percentual weight on F675W 1/RMS image (within ISOphotal Area).
99	irms_F706W	Percentual weight on F706W 1/RMS image (within ISOphotal Area).
100	irms_F737W	Percentual weight on F737W 1/RMS image (within ISOphotal Area).
101	irms_F768W	Percentual weight on F768W 1/RMS image (within ISOphotal Area).
102	irms_F799W	Percentual weight on F799W 1/RMS image (within ISOphotal Area).
103	irms_F830W	Percentual weight on F830W 1/RMS image (within ISOphotal Area).
104	irms_F861W	Percentual weight on F861W 1/RMS image (within ISOphotal Area).
105	irms_F892W	Percentual weight on F892W 1/RMS image (within ISOphotal Area).
106	irms_F923W	Percentual weight on F923W 1/RMS image (within ISOphotal Area).
107	irms_F954W	Percentual weight on F954W 1/RMS image (within ISOphotal Area).
108	irms_J	Percentual weight on J 1/RMS image (within ISOphotal Area).
109	irms_H	Percentual weight on H 1/RMS image (within ISOphotal Area).
110	irms_KS	Percentual weight on KS 1/RMS image (within ISOphotal Area).
111	irms_F814W	Percentual weight on F814W 1/RMS image (within ISOphotal Area).
112	irms_OPT_Flag	Optical quality flag. Number of optical filters with PercW < 0.8.
113	irms_NIR_Flag	NIR quality flag. Number of NIR filters with PercW < 0.8.

Table D1. Example of the typical SExtractor configuration used to derive the ALHAMBRA photometric catalogues. Asterisked parameters may vary among CCDs.

Parameter	Setting	Comment
ANALYSIS_THRESH	1.3*	Limit for isophotal analysis σ
BACK_SIZE	256	Background mesh in pixels
BACK_FILTERSIZE	5	Background filter
BACKPHOTO_THICK	102	Thickness of the background LOCAL annulus
BACKPHOTO_TYPE	LOCAL	Photometry background subtraction type
CATALOG_NAME	STDOUT	Output to pipe instead of file
CATALOG_TYPE	ASCII	Output type
CLEAN	Y	Clean spurious detections
CLEAN_PARAM	1	Cleaning efficiency
CHECKIMAGE_TYPE	SEGMENTATION	Output image type
DETECT_MINAREA	8*	Minimum number of pixels above threshold
DEBLEND_MINCONT	0.0002	Minimum contrast parameter for deblending
DEBLEND_NTHRESH	64	Number of deblending sub-thresholds
DETECT_THRESH	1.35*	Detection threshold in σ
DETECT_TYPE	CCD	Detector type
FILTER	Y	Use filtering
FILTER_NAME	tophat_3.0_3x3.conv	Filter for detection image
GAIN	57.68*	Gain is 1 for absolute RMS map
MAG_GAMMA	4.0	Gamma of emulsion
MAG_ZEROPOINT	0.*	Magnitude zero-point
MEMORY_PIXSTACK	2600000	Number of pixels in stack
MEMORY_BUFSIZE	4600	Number of lines in buffer
MEMORY_OBJSTACK	15000	Size of the buffer containing objects
MASK_TYPE	CORRECT	Correct flux for blended objects
PARAMETERS_NAME	ColorPro.param	Fields to be included in output catalogue
PHOT_APERTURES	14.0	MAG_APER aperture diameter(s) in pixels
PHOT_AUTOPARAMS	2.5,3.5	MAG_AUTO parameters: <Kron_fact>,<min_radius>
PIXEL_SCALE	0.221	Size of pixel in arcsec
SATUR_LEVEL	50000	Level of saturation
SEEING_FWHM	0.86*	Stellar FWHM in arcsec
STARNNW_NAME	default.nnw	Neural-Network_Weight table filename
WEIGHT_TYPE	MAP_WEIGHT	Set weight image type

Table D2. Effective surveyed area. The definition of the effective area is provided in Section 3.5.3.

Field name	Eff. area [deg^2]	Field name	Eff. area [deg^2]
ALHAMBRA_F02P01C01	0.0580	ALHAMBRA_F06P01C01	0.0593
ALHAMBRA_F02P01C02	0.0584	ALHAMBRA_F06P01C02	0.0583
ALHAMBRA_F02P01C03	0.0540	ALHAMBRA_F06P01C03	0.0585
ALHAMBRA_F02P01C04	0.0582	ALHAMBRA_F06P01C04	0.0582
ALHAMBRA_F02P02C01	0.0596	ALHAMBRA_F06P02C01	0.0587
ALHAMBRA_F02P02C02	0.0506	ALHAMBRA_F06P02C02	0.0587
ALHAMBRA_F02P02C03	0.0538	ALHAMBRA_F06P02C03	0.0572
ALHAMBRA_F02P02C04	0.0586	ALHAMBRA_F06P02C04	0.0589
ALHAMBRA_F03P01C01	0.0586	ALHAMBRA_F07P03C01	0.0587
ALHAMBRA_F03P01C02	0.0589	ALHAMBRA_F07P03C02	0.0590
ALHAMBRA_F03P01C03	0.0578	ALHAMBRA_F07P03C03	0.0576
ALHAMBRA_F03P01C04	0.0592	ALHAMBRA_F07P03C04	0.0587
ALHAMBRA_F03P02C01	0.0592	ALHAMBRA_F07P04C01	0.0589
ALHAMBRA_F03P02C02	0.0577	ALHAMBRA_F07P04C02	0.0566
ALHAMBRA_F03P02C03	0.0569	ALHAMBRA_F07P04C03	0.0580
ALHAMBRA_F03P02C04	0.0590	ALHAMBRA_F07P04C04	0.0590
ALHAMBRA_F04P01C01	0.0589	ALHAMBRA_F08P01C01	0.0588
ALHAMBRA_F04P01C02	0.0590	ALHAMBRA_F08P01C02	0.0590
ALHAMBRA_F04P01C03	0.0569	ALHAMBRA_F08P01C03	0.0577
ALHAMBRA_F04P01C04	0.0589	ALHAMBRA_F08P01C04	0.0587
ALHAMBRA_F05P01C01	0.0595	ALHAMBRA_F08P02C01	0.0585
ALHAMBRA_F05P01C02	0.0594	ALHAMBRA_F08P02C02	0.0583
ALHAMBRA_F05P01C03	0.0588	ALHAMBRA_F08P02C03	0.0558
ALHAMBRA_F05P01C04	0.0594	ALHAMBRA_F08P02C04	0.0576

[1]*IAA–CSIC, Glorieta de la astronomía S/N. E-18008, Granada, Spain*
[2]*Centro de Estudios de Física del Cosmos de Aragón (CEFCA), Plaza San Juan 1, E-44001 Teruel, Spain*
[3]*Instituto de Física de Cantabria (CSIC–UC), E-39005 Santander, Spain*
[4]*Unidad Asociada Observatori Astronómic (IFCA – Universitat de Valéncia), Valencia, Spain*
[5]*Institute for Computational Cosmology, Department of Physics, Durham University, South Road, Durham DH1 3LE, UK*
[6]*Space Telescope Science Institute, Baltimore, MD, USA*
[7]*Physics and Astronomy Department, University of Missouri, Columbia, MO 65211, USA*
[8]*Observatório Nacional–MCT, Rua José Cristino 77, CEP 20921-400, Rio de Janeiro–RJ, Brazil*
[9]*Instituto de Astrofísica de Canarias, Vía Láctea s/n, La Laguna, Tenerife 38200, Spain*
[10]*GEPI, Paris Observatory, 77 av. Denfert Rochereau, F-75014 Paris, France*
[11]*University Denis Diderot, 4 Rue Thomas Mann, F-75205 Paris, France*
[12]*Department of Theoretical Physics, University of the Basque Country UPV/EHU, Bilbao, Spain*
[13]*Departamento de Física Atómica, Molecular y Nuclear, Facultad de Física, Universidad de Sevilla, Spain*
[14]*Departamento de Astrofísica, Facultad de Física, Universidad de la Laguna, Spain*
[15]*Departamento de Astronomía, Pontificia Universidad Católica, Santiago, Chile*
[16]*Departament d'Astronomía i Astrofísica, Universitat de Valencia, E-46100 Valencia, Spain*
[17]*Observatori Astronomic de la Universitat de Valencia, E-46071 Valencia, Spain*

This paper has been typeset from a TEX/LATEX file prepared by the author.